Renewable Energy 173 (2021) 422–441

Contents lists available at ScienceDirect

Renewable Energy

journal homepage: www.elsevier.com/locate/renene

Effect of airfoil shape on power performance of vertical axis wind turbines in dynamic stall: Symmetric Airfoils

M. Rasoul Tirandaz [a], Abdolrahim Rezaeiha [b, c, *]

[a] Sharif University of Technology, Tehran, Iran
[b] KU Leuven, Leuven, Belgium
[c] Eindhoven University of Technology, Eindhoven, the Netherlands

ARTICLE INFO

Article history:
Received 5 January 2021
Received in revised form
16 March 2021
Accepted 30 March 2021
Available online 2 April 2021

Keywords:
Smart rotor design
Unsteady aerodynamics
Morphing airfoil
Computational fluid dynamics (CFD)
Floating offshore wind turbine (FOWT)
Building-integrated wind turbine

ABSTRACT

The current design of vertical axis wind turbines (VAWTs) suffers from inevitable change in tip speed ratio, λ, in variant wind conditions due to fixed rotor speed. At relatively high wind speeds, which are promising due to high wind power potential, VAWTs operate at low λ with poor power coefficient. Morphing airfoils can be a potential solution by modifying the airfoil shape to optimal at each λ. The optimal airfoil shape for VAWTs at low λ, where dynamic stall is present, has not yet been studied in the literature, therefore, the present study addresses this gap by focusing on this regime to serve as a step towards designing morphing airfoils for VAWTs by identifying the optimal airfoil shape at low λ. The present study performs a combined analysis of three shape defining parameters, namely the airfoil maximum thickness and its position as well as the leading-edge radius, to reveal the overall design space. The analysis is based on 252 high-fidelity transient CFD simulations of 126 identical airfoil shapes. The simulations are verified and validated with three experiments. The results show that the three shape defining parameters have a fully coupled impact on the turbine power and thrust coefficients. When λ reduces from 3.0 to 2.5, the optimal airfoil changes from NACA0018−4.5/2.75 to NACA0024−4.5/3.5, that is increasing the maximum thickness from 18%c to 24%c and shifting its position from 27.5%c to 35%c, while the leading-edge radius index, I, remains 4.5. In general, reducing I from the default value of 6.0 to 4.5 is found to increase the turbine C_P.

1. Introduction

1.1. The state-of-the-art and research gaps

Airfoil shape plays a crucial role in overall performance of aerodynamic bodies and this has resulted in extensive research to design dedicated airfoil shapes based on the target design condition. Some examples are for helicopters [1–3], aircrafts [4–7], micro-air vehicles [8,9], propellers [10–12], gas turbine blades [13,14], fans/compressors [15–18] and wind turbines [19–27].

For horizontal axis wind turbines (HAWTs), a few examples of dedicated airfoil series are *S8xx series* by NREL, USA [25], *FFA W-xxx series* by FOI, Sweden [28], *Risø-A1-xxx* and also *B-* and *P-series* by Risø, DTU, Denmark [20–22], and *DU xx-W-xxx series* by TU Delft, the Netherlands [26,27].

In contrast, vertical axis wind turbines (VAWTs) originally borrowed their airfoil shapes from helicopter industry, i.e. the typical symmetric NACA four-digit airfoil series, and characterization and optimization of airfoil shape for VAWTs have received much less attention [29,30]. The pioneering works on the analysis of the airfoil shape for VAWTs are the works by Kato et al. [31], Klimas [32], Galbraith et al. [33], Claessens [34] and Ferreira and Geurts [35]. To this date, the commercial VAWTs are not yet widely benefitting from dedicated airfoil shapes and this has contributed to their comparatively low aerodynamic performance against their modern horizontal axis counterparts [36–41].

The blade of a VAWT operates in a wide range of positive/negative angles of attack, α. Due to the cyclic variations of α, the blade experiences unsteady separation. At low tip speed ratios (λ), the blade could experience both pre- and post-stall regimes in a complex transient manner. In that case, dynamic stall would happen resulting in the well-known hysteresis effects on the aerodynamic loads [42–46]. This further sophisticates the blade

* Corresponding author. Sharif University of Technology, Tehran, Iran.
E-mail addresses: mr.tirandaz@alum.sharif.edu (M.R. Tirandaz), a.rezaeiha@tue.nl (A. Rezaeiha).

https://doi.org/10.1016/j.renene.2021.03.142

Nomenclature

α	Angle of attack [ ]
α_{ss}	Static stall angle [ ]
θ	Azimuth angle [ ]
λ	Tip speed ratio, $R\Omega/U_\infty$ [−]
ν	Kinematic viscosity of air [m^2/s]
σ	Solidity, nc/d [−]
Ω	Turbine rotational speed [rad/s]
c	Airfoil chord length [m]
C_m	Instantaneous moment coefficient, $M/(qAR)$ [−]
C_P	Power coefficient, $P/(qAU_\infty)$ [−]
C_T	Turbine thrust coefficient, $T/(qA)$ [−]
I	Airfoil leading-edge radius index [−]
M	Turbine moment [Nm]
n	Number of blades [−]
P	Turbine output power [W]
q	Dynamic pressure [Pa]
R	Turbine radius [m]
Re_c	Chord-based Reynolds number, $cU_\infty\sqrt{1+\lambda^2}/\nu$ [−]
r_{LE}	Airfoil leading-edge radius [% c]
T	Turbine thrust force [N]
t/c	Airfoil relative maximum thickness [%]
U_∞	Freestream velocity [m/s]
u	Instantaneous streamwise velocity [m/s]
v	Instantaneous lateral velocity [m/s]
$V_{tan,n}$	Dimensionless instantaneous tangential velocity, $(ucos(\theta)+vsin(\theta))/U_\infty$
V_{rel}	Relative velocity [m/s]
xt/c	Chordwise-position of airfoil maximum thickness [%]
AD	Absolute deviation
TI	Total turbulence intensity [%]

aerodynamics of VAWTs. As a result of this, not a single design condition exists for VAWTs so that a single optimal airfoil shape can be designed for and this has significantly hindered the airfoil optimization efforts for VAWTs.

Instead, a comprehensive characterization of the parameters defining the airfoil shape would provide a fundamental understanding of their individual/combined influences on the power performance of VAWTs. In addition, the developed knowledge would be a step forward towards designing improved airfoil shapes for VAWTs. However, such comprehensive knowledge on the impact of the airfoil shape defining parameters on the aerodynamic performance of VAWTs is currently not sufficiently developed in the literature. Table 1 lists an overview of the literature on characterization of airfoil shape for VAWTs. In the table, summary information on the investigated airfoil shapes (number of studied shapes, studied parameters and their range), the method of the study (numerical/experimental) and the turbine geometrical and operational characteristics in the study (turbine solidity, tip speed ratio and Reynolds number) are presented.

Among the presented literature, the momentum-based models, such as the multiple streamtube models, have been employed by Healy [47], Migliore [48], Kirke and Lazauskas [49], Bedon et al. [50], Jafari et al. [51], Fernández et al. [52]. However, such models are fundamentally developed for HAWTs and do not correspond to the underlying physics of VAWTs and their inaccuracies to predict the power performance of VAWTs are already known in the literature, see Ref. [53].

Among the high-fidelity CFD studies, a few, e.g. Ref. [54], randomly selected several studies, therefore, no insight on the influence of the airfoil shape defining parameters could not be developed. Detailed analysis of the literature shows that, on the one hand, the majority of the systematic studies are mainly focused on

Table 1
Overview of the literature on characterization of airfoil shape for VAWTs.

Reference		Airfoil shape			Method	Turbine conditions		
Date	Author	# Cases	Parameters	Range [%]		σ	λ	Re [× 10^5]
1978	Healy [47]	4	t/c	9–18	Num (MST)	0.05–0.15	2.25–6	1.1–23.3
1983	Migliore [48]	10	t/c	12–18	Num (MST)	0.07–0.21	2–12	30
1991	Kirke and Lazauskas [49]	5	t/c, C	t/c: 12–21, C: 0–4	Num (DMST)	0.19–0.76	0.12–4.25	2
2012	Mohamed [54]	20	–	t/c: 5.9–30.1 xt/c: 20.8–42.2 C: 0–4.3 xC: 0–82.3	Num (CFD)	0.1–0.25	2–10	–
2014	Ragni et al. [62]	5	–	t/c: 15–25	Exp (WT), Num (PC)	0.07–0.13	3–7	3.5, 7, 10
2015	Nguyen et al. [55]	4	t/c	12–21	Num (CFD)	0.25	2.33	1.6–3.8
2015	Bedon et al. [50]	6	t/c	15–25	Num (DMST)	0.16	1.5–8.5	1–3
2016	Torabi Asr et al. [63]	6	t/c, C	t/c: 18–24, C: 0–4	Num (CFD)	0.33	1.2–4.2	0.67–1.87
2016	Chen et al. [60]	16	t/c, I, xt/c	t/c: 15–24 I: 0–9 [-] xt/c: 20–50	Num (CFD)	0.6	0.5–4	–
2017	Subramanian et al. [56]	4	t/c	12–30	Num (CFD)	0.33, 0.5	1.0–2.5	5.1–9.8
2018	Wang et al. [61]	64	t/c, xt/c, C, xC	t/c: 6–18 xt/c: 15–40 C: 0.61–3.81 xC: 0–5	Num (CFD)	0.5	1.5–5	1.2–3.4
2018	Jafari et al. [51]	6	–	t/c: 19.6–24	Num (DMST)	0.2–0.6	1.0–12	3.6–31.4
2018	Fernández et al. [52]	34	–	t/c: 12–25 C: 0–8 xC: 0, 4	Num (DMST)	0.25–0.5	2.5–5	0.84–1.6
2019	Song et al. [64]	10	r_{LE}	1–9	Num (CFD)	0.68	0.5–3	2.9–8.2
2020	Song et al. [57]	4	t/c	12–21	Num (CFD)	0.68	0.5–3	2.9–8.2
2020	Mazarbhuiya and Biswas [58]	5	t/c	22.5–37.5	Num (CFD)	0.3	1.6–2.8	0.49–0.77
2020	Jain and Saha [59]	5	t/c	9–21	Num (CFD)	0.16	2	1.25

Note: MST (multiple streamtube model); DMST (double MST); WT (wind tunnel); PC (panel code); C (maximum camber); xC (chordwise position of maximum camber).

Table 2
Characteristics of the reference turbine.

Turbine type	Darrieus H-type
n	1
d	1 m
σ	0.06
Airfoil shape	NACA0018-63 (i.e. original NACA0018) - $t/c = 18\%$ - $xt/c = 30\%$ - $I = 6$
c	0.06 m
U_∞	9.3 m/s
Ω	46.5, 55.8 rad/s
λ	2.5, 3.0
Re_c [$\times 10^5$]	1.03, 1.20
TI	5%

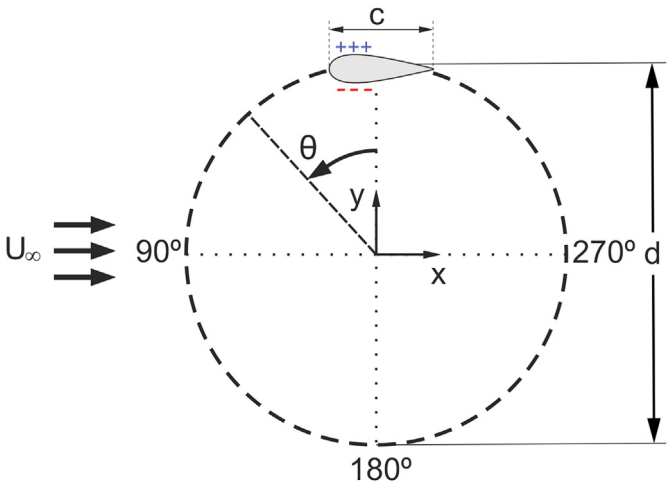

Fig. 1. Top view of the reference turbine (not to scale). The (+) and (−) signs denote the pressure and suction sides for $0^\circ \leq \theta < 180^\circ$.

the impact of a single airfoil shape defining parameter, mostly the airfoil relative maximum thickness (t/c), see for example the works of Nguyen et al. [55], Subramanian et al. [56], Song et al. [57], Mazarbhuiya and Biswas [58], Jain and Saha [59]. This is while the other shape defining parameters are kept fixed in the study. Note that some parameters such as the chordwise position of maximum thickness and the leading-edge radius has received much less attention.

These factors limit the generality of the provided conclusions mainly because the airfoil defining shape parameters could have coupled impacts on the boundary layer events along the blade, the stall behavior, and the resultant aerodynamic loading. Therefore, isolated analysis of one parameter, while the others are kept constant, might be misleading by not presenting the global picture.

On the other hand, dynamic stall is an important flow phenomenon associated with VAWTs and its occurrence at low λ is inevitable as the typical design of VAWTs does not incorporate variable-speed control. Furthermore, except the turbine start up, low λ corresponds to relatively high wind speeds, where the available power potential is significant, however, the turbine is unable to extract. Thus, characterizing the impact of the airfoil shape focusing on this operational regime is of high importance as future designs can focus on morphing blades adapting the airfoil shape to the identified optimal shape at this regime to maximize the power output. However, to the best of our knowledge, no previous study has focused on this particular regime.

In addition, the number of the airfoil shapes per study in systematic high-fidelity CFD studies is limited to very few shapes, except the works of Chen et al. [60] and Wang et al. [61], where larger number of shapes were investigated, although still the focus was not on the dynamic stall regime.

1.2. Novelty and objectives

Three main gaps are identified in the literature of airfoil studies for VAWTs, see Table 1, which are briefed as follows:

i. The first gap is related to the common decoupled analysis of the impact of the airfoil shape defining parameters, meaning that a parameter is studied while having the rest fixed and deriving conclusions accordingly.
ii. The second gap is associated with deriving conclusions based on limited number of the airfoil shapes studied.
iii. The third gap is with respect to the regime of study, that is the low tip speed ratios including dynamic stall, which has not been the focus of the study mainly because the majority of the studies have focused on the optimal regime. However, in order to design morphing airfoil shapes adapting their shape according to the turbine tip speed ratio, all the relevant tip speed ratios would be important and cannot be neglected.

To address these gaps, the present study has the following aim and objectives:

i. To understand the individual/combined impact of the airfoil shape defining parameters on the turbine power and thrust coefficients (C_P and C_T) using a coupled analysis, meaning that all the possible combinations of the studied parameters within a relevant range will be studied.
ii. To drive generalizable conclusions by basing that on an extensive systematic analysis including 252 transient simulations corresponding to 126 identical airfoil shapes (6 different airfoil relative maximum thickness t/c, 7 different chordwise position of the airfoil maximum thickness xt/c, and 3 different leading-edge radius indexes I) at 2 different tip speed ratios, λ, performed
iii. Identifying the optimal airfoil shapes at low tip speed ratios, where the dynamic stall complicates the blade aerodynamics.

The focus of the work will be on symmetric airfoil shapes

Table 3
Details of computational domain, gird and boundary conditions.

Computational domain (see Fig. 2a)	30 d × 30 d (d: turbine diameter)
Computational grid (see Fig. 2b–e)	302,815 quadrilateral cells, 800 cells around the airfoil circumference, max $y^+ < 2.5$
Boundary conditions	*Inlet*: uniform normal velocity (TI = 5%, turbulence length scale = d); *Outlet*: zero static gauge pressure; *Side boundaries*: symmetry; *Walls*: no-slip

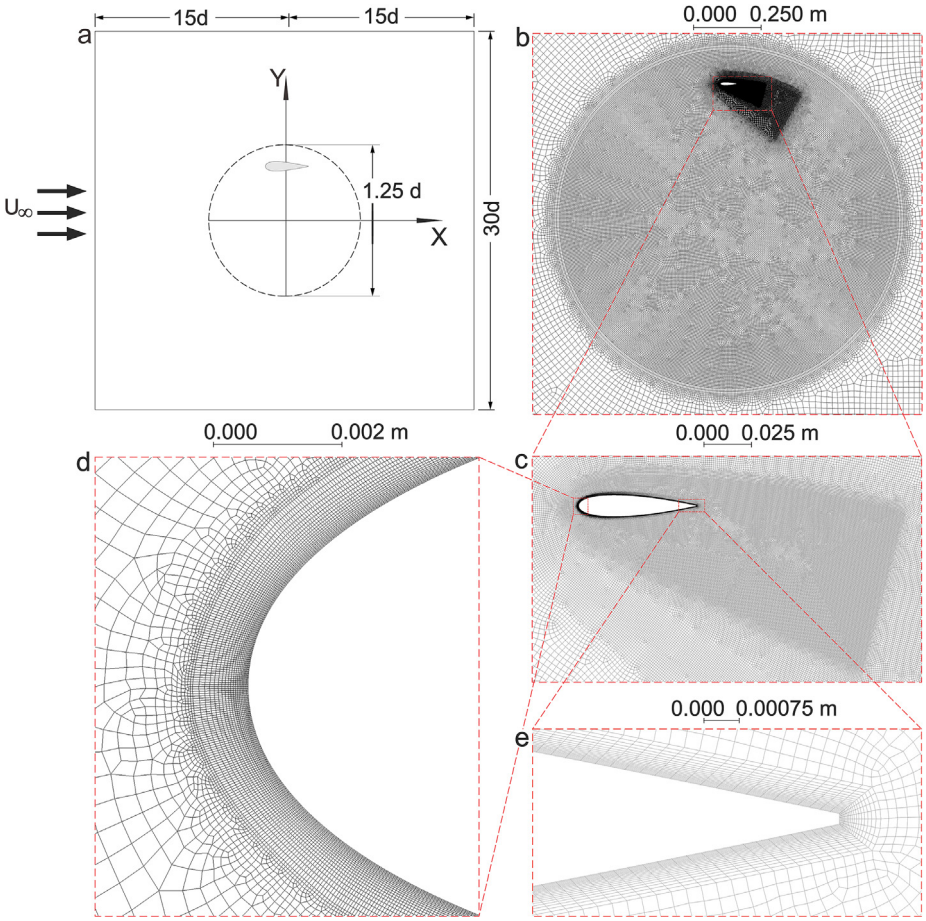

Fig. 2. Schematic of (a) the computational domain (not to scale); (b–e) grid.

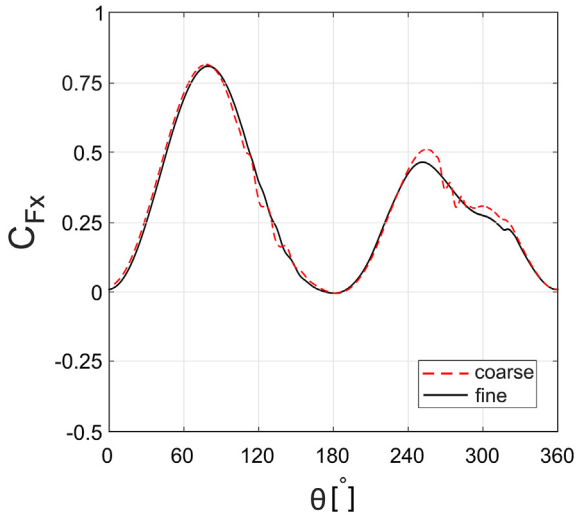

Fig. 3. Grid sensitivity analysis for the reference turbine: streamwise force coefficient during the last turbine revolution.

modified based on the popular NACA four-digit airfoil series. The analysis is based on unsteady Reynolds-Averaged Navier-Stokes (URANS) approach, already extensively validated with experimental data.

The provided conclusions will help to characterize the influence of airfoil shape defining parameters on power performance of VAWTs and to identify the optimal airfoil shapes at low tip speed ratios to support designing morphing airfoil shapes for VAWTs.

1.3. The regime of study

Unlike the more common HAWTs, the current design of VAWTs have fixed rotor rotational speed (excl. the start-up). Therefore, their tip speed ratio is inevitably varying within a wide range due to the changes in the incoming flow velocity. More specifically, at higher wind speeds, which are theoretically more interesting due to the higher available wind power, they would operate in low tip speed ratios. However, due to the occurrence of dynamic stall, their power performance dramatically drops, and this has a significant impact on their annual energy production (AEP). Thus, towards improving the design of smart VAWT through identifying the optimal airfoil shapes for morphing blades, the present study focuses on low tip speed ratios.

1.4. Paper outline

This paper is organized as follows: Sec. 2 gives a brief overview of the computational settings and parameters. The solution verification and validation studies are also discussed. Sec. 3 describes the studied airfoil shapes, the equations to generate the modified airfoils and the list of the test cases. The results are presented and discussed in Sec. 4, where in 2 sub-sections the impact of each parameter is separately discussed and then a sub-section discussed

Table 4
Validation studies: details of the experiments and the absolute deviation (AD) between CFD and experiment in %. Experimental uncertainty (ExUn) is also reported in % where available.

Validation study	Turbine and test settings				Validation parameter	Comparison of CFD and Exp.				
	λ	σ	k	Re [$\times 10^5$]						
1	2.0	0.125	0.125	0.5	θ	90°	108°	133°	158°	223°
					AD	31.1	11.6	4.5	16.6	7.4
					ExUn	20.2	11.0	12.5	17.5	31.1
2	4.5	0.12	0.06	1.7	x/R	1.5	2.0	2.5	3.0	3.5
					AD (u)[a]	6.8	8.0	9.8	11.7	12.3
					AD (v)[a]	2.8	2.5	2.3	2.2	2.3
3	2.04–3.08	0.25	0.082	0.91–1.8	λ	2.04	2.33	2.51	2.64	3.08
					AD (C_P)	3.42	10.7	0.5	6.8	23.2

[a] Averaged along the lateral direction ($-0.75 \leq y/d \leq 0.75$).

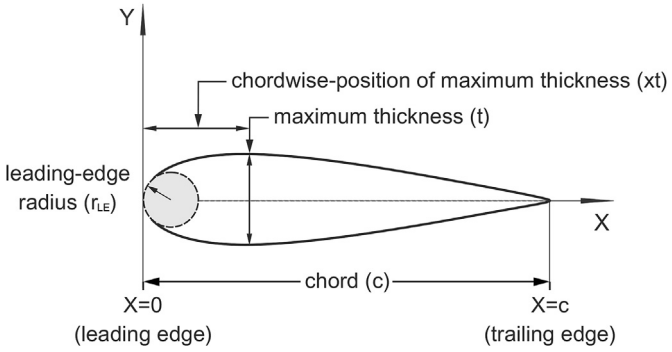

Fig. 4. Symmetric airfoil shape parameters.

their combined impact. Finally, a last sub-section presents an aerodynamic analysis of the optimal airfoil shapes. Discussion and conclusions are given in Sec. 5 and 6.

2. Computational settings and parameters

2.1. Turbine characteristics

The reference turbine is a one-bladed Darrieus (lift-based) H-type VAWT with the geometrical and operational characteristics given in Table 2. The location of blade-spoke connection is c/2. A schematic of the reference turbine is depicted in Fig. 1. The reference turbine is a simplified version of the turbine in the experiment by Tescione et al. [65], which is used for one of the validation studies performed by the authors [66]. The simplified version excludes the shaft and the spokes and only has one blade to reduce the computational cost associated with the large number of simulations in the present study, i.e. in total 252 transient simulations. Please note that this simplification is believed to have negligible impact on the conclusions of this study because the influence of the excluded components has been already studied and known in our previous works [67,68]. For example, regarding the number of blades, we have found that the power performance of low-solidity VAWTs is weakly dependent on the number of blades within a wide range of tip speed ratios. Therefore, in the present study, a one-bladed low-solidity turbine is selected, which will be highly beneficial considering the computational cost.

The rest of the turbine geometrical and operational characteristics are based on our previous studies on characterization of VAWTs [68,69].

2.2. Computational settings

The simulations are based on solving the incompressible URANS simulations together with the four-equation transition SST turbulence model, all with the second-order spatial/temporal discretization. The SIMPLE scheme is used for the pressure-velocity coupling. The employed solver is the commercial CFD package ANSYS Fluent v2019R2. Table 3 lists the rest of the computational settings regarding the computational domain, grid and boundary conditions. Fig. 2 shows the schematic of the computational domain and different regions of the computational grid.

The choice of the turbulence model in this work is based on an extensive critical analysis of seven commonly used Reynolds-averaged eddy-viscosity turbulence models against three different dissimilar experiments [66] and two more advanced scale-resolving simulations [45,70]. The conclusions of these studies showed that the four-equation transition SST turbulence models is the best-performing eddy-viscosity model for URANS simulation of complex unsteady aerodynamics of VAWTs in dynamic stall.

The transient simulations of turbines utilize an azimuthal increment of $d\theta = 0.1°$, corresponding to an absolute time-step of $3.75339546 \times 10^{-5}$ s and $3.12782955 \times 10^{-5}$ s at tip speed ratios of 2.5 and 3.0. This azimuthal increment results in 3600 time-steps per turbine revolution. The value of $d\theta$ is selected based on the best-practice guidelines for CFD simulations of VAWTs, where the minimum requirement at low tip speed ratios to have time-step independent results was found to be 0.1°.

A number of 20 iterations per time-step is employed to ensure that the scaled residuals drop below 10^{-5}. In total, 20 turbine revolutions, i.e. 72,000 time-steps, are simulated to reach statistical convergence of the transient simulations. Therefore, the results presented in this work correspond to the 21st turbine revolution. The convergence criterion is also based on the best-practice guidelines for CFD simulations of VAWTs [71].

Table 5
Range of studied airfoil shape parameters.

Relative maximum thickness, *t/c* [%]	10, 12, 15, 18, 21, 24
Chordwise position of maximum thickness, *xt/c* [%]	20, 22.5, 25, 27.5. 30, 35, 40
Leading-edge radius index, *I*	4.5, 6.0, 7.5

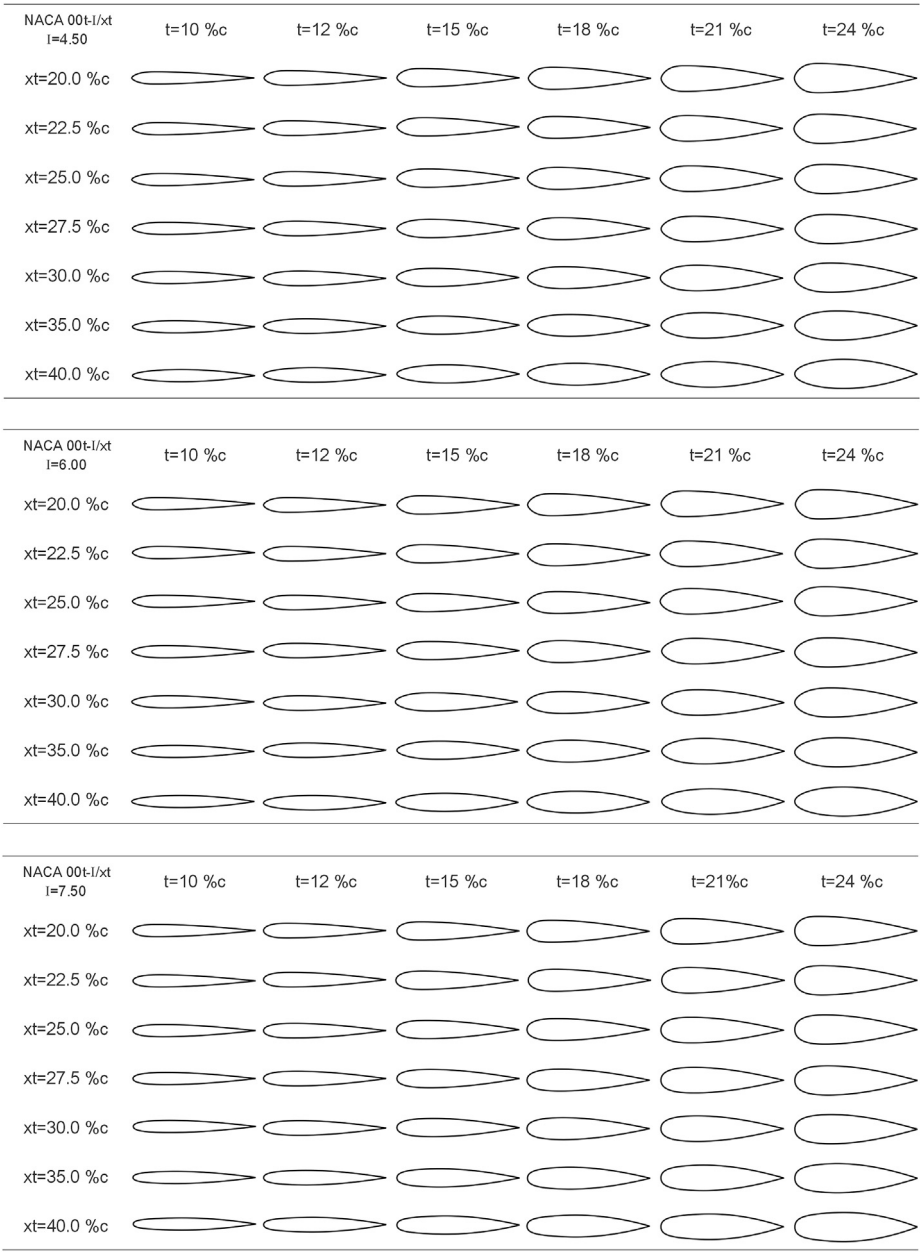

Fig. 5. Studied airfoil profiles.

2.3. Solution verification and validation

The domain size, the azimuthal increment, and the convergence criterion are based on the best-practice guidelines for CFD simulations of VAWTs [71]. The selection of the domain type is because our previous comparison with 2.5D URANS simulations showed negligible systematic difference [69].

The grid is selected based on a grid sensitivity analysis performed for the reference turbine, where the employed grid, coarse gird, is compared with a grid uniformly doubled in all directions, resulting in 1,211,260 cells for the fine grid. Fig. 3 shows the turbine streamwise force coefficient (C_{Fx}) during the last turbine revolution for the coarse and fine grids. The mean and maximum absolute deviation in C_{Fx} between the two grids is 0.01 and 0.07. The Grid Convergence Index (GCI) by Roache [72] is employed to further analyze the grid independence of the results. The GCI^{coarse} calculated using the turbine thrust coefficient, employing a safety factor of 1.25, for the coarse-fine grid pair is 0.0073, which is 2.45% of the Richardson's extrapolated value. Further details of the grid sensitivity analysis for the reference turbine is given in Ref. [73].

The CFD simulations are validated against three different experiments. The three turbines employed in the validations have different properties (i. e. different number of blades, solidity, airfoil shape, tip speed ratio, and Reynolds number). The experiments are performed in different wind tunnels and they reported dissimilar flow or turbine quantities. These variety helps to ensure the accuracy of the present CFD simulations. A brief overview of the three validation studies is given below:

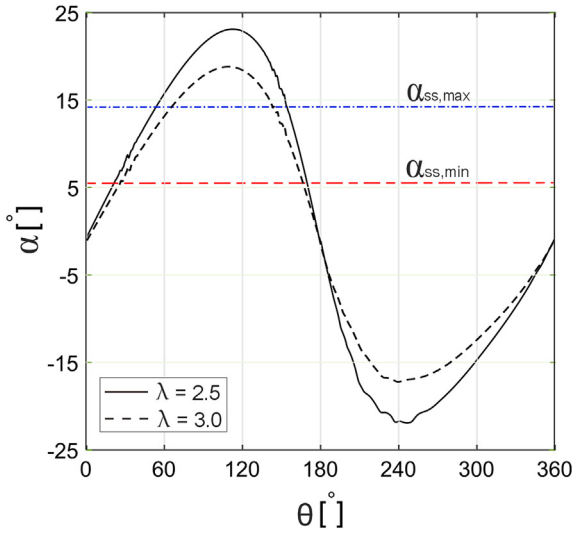

Fig. 6. Angle of attack vs azimuth for tip speed ratios of 2.5 and 3.0. The $\alpha_{ss,min}$ and $\alpha_{ss,max}$ are the minimum and maximum static stall angles for studied airfoils based on Xfoil.

1) Validation study 1: planar PIV measurements by Ferreira et al. [42] for a one-bladed VAWT equipped with NACA0015 airfoil operating in dynamic stall is employed for validation study 1. In the experiment, the blade vorticity evolution was analyzed.
2) Validation study 2: stereoscopic PIV measurements by Tescione et al. [65] for a two-bladed VAWT equipped with NACA0018 airfoil operating in optimal regime is employed for validation study 2. The experiment measured the streamwise and lateral velocities in the turbine near wake.
3) Validation study 3: C_P measurements by Castelli et al. [74] for a three-bladed VAWT equipped with NACA0021 airfoil operating at a wide range of tip speed ratios is used for validation study 3.

Table 4 presents details of the test and turbine settings and the absolute deviation (AD) between CFD and experiment in %. Experimental uncertainty (ExUn) is also reported in % where available. For brevity, the details of the validation studies are not repeated here, and the reader is referred to Refs. [66]. For the three validation studies, acceptable agreement between the CFD and the experiment was observed.

3. Airfoil shapes

3.1. List of test cases

In the present study, the three main parameters defining the shape of the symmetric NACA four-digit airfoil series, shown in Fig. 4, are modified within the ranges given in Table 5.

The selected ranges represent the most practical regimes for the three parameters, since the typical range for airfoil maximum thickness is between 10% and 24%; a chordwise position of maximum thickness greater than 40% results in an undesirable airfoil shape; and a leading edge with a radius index of smaller than 4.5 and larger than 7.5 would be too sharp and too blunt, respectively. In total, 126 airfoil shapes are generated for the analysis. The generated airfoil shapes are shown in Fig. 5. The modification of the airfoil shapes and the related equations are presented in Sec. 3.2.

3.2. Modification of airfoil coordinates

The airfoil shape coordinates (X, Y) for the modified symmetric NACA four-digit airfoil series are defined using Eq. (1) [75]. Taking the airfoil chord as the X-axis ranging from 0 to 1, the equation will provide the ordinates Y using two separate equations, (1) for X ranging from the leading edge to the location of the airfoil maximum thickness ($0 \le X < xt/c$); and (2) for X ranging from the location of the airfoil maximum thickness to the trailing edge ($xt/c < X \le 1$).

$$\begin{cases} \mp Y_1 = 0.5\left(a_0\sqrt{X} + a_1 X + a_2 X^2 + a_3 X^3\right), & 0 \le X < xt/c \\ \mp Y_2 = d_0 + d_1(1-X) + d_2(1-X)^2 + d_3(1-X)^3, & xt/c < X \le 1 \end{cases} \quad (1)$$

The four coefficients d_0, d_1, d_2 and d_3, are determined as follow, see Eq. (2)–5:

$$d_0 = \frac{\text{trailing edge gap}}{2} \quad (2)$$

Note that the standard NACA four-digit airfoil has a small gap at the trailing edge, to about 1% t/c. In case of a closed-gap trailing edge, d_0 is set equal to zero [76]. The coefficient d_1 is the trailing-edge slope and can be expressed as a function of t/c and xt/c, see Eq. (3):

$$d_1 = \left(15.83333\left(\frac{xt}{c}\right)^3 - 2.17857\left(\frac{xt}{c}\right)^2 - 0.240476\left(\frac{xt}{c}\right)^2 + 1.009\right)(t/c) \quad (3)$$

The coefficients d_2 and d_3 can be computed using Eq. (4)–5:

$$d_2 = \frac{3[t/c - 2d_0 - 2d_1(1-xt/c)]}{2(1-xt/c)^2} + \frac{d_1}{1-xt/c} \quad (4)$$

$$d_3 = \frac{-d_1}{3(1-xt/c)^2} + \frac{2d_2}{3(1-xt/c)} \quad (5)$$

Having I, the coefficient a_0 is calculated using Eq. (6):

$$a_0 = 0.296904\frac{I}{6} \quad (6)$$

Having the xt/c and the coefficient d_1, a new parameter p is defined, see Eq. (7), which is used to calculate the coefficients a_1, a_2 and a_3 using Eq. (8)–10:

$$p = \frac{0.2(1-xt/c)^2}{0.588 - 2d_1(1-xt/c)} \quad (7)$$

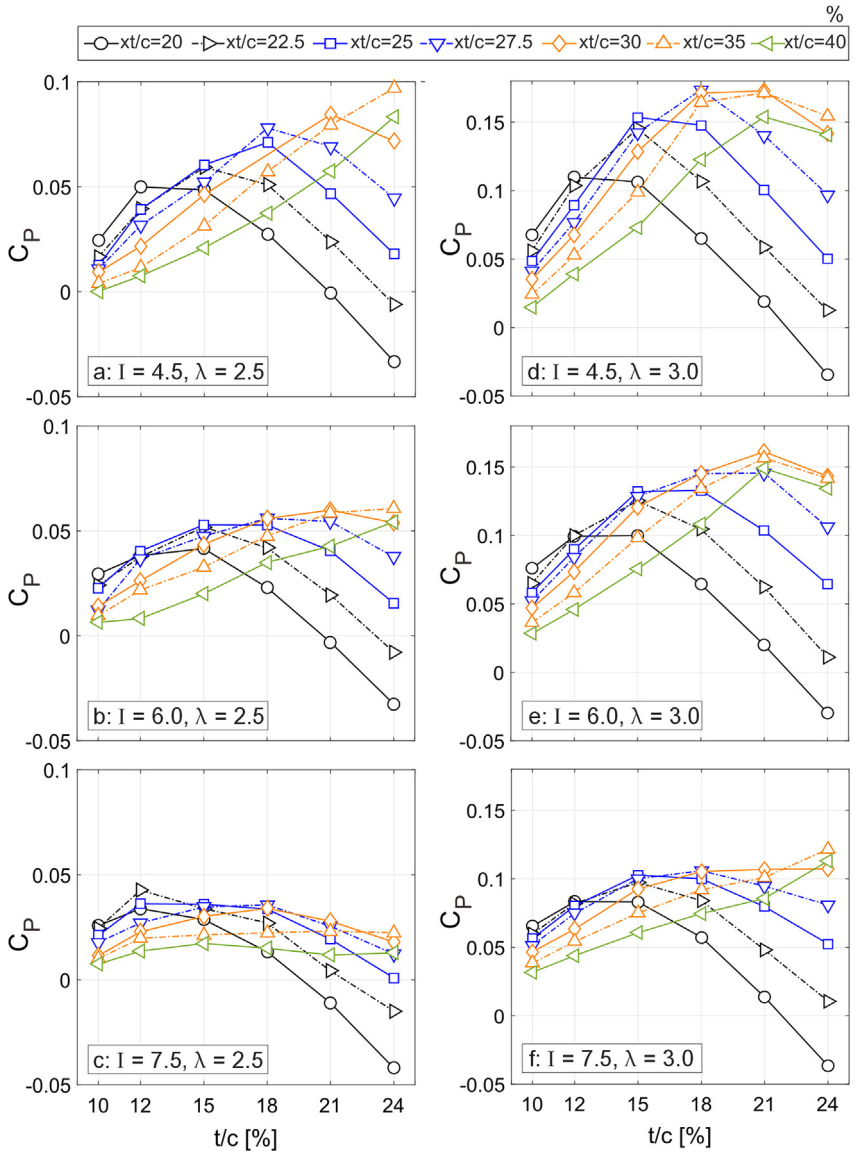

Fig. 7. Turbine power coefficient versus airfoil relative maximum thickness.

$$a_1 = \left(\frac{0.3}{xt/c}\right) - \left(\frac{15a_0}{8\sqrt{xt/c}}\right) - \left(\frac{xt/c}{10p}\right) \tag{8}$$

$$a_2 = -\left(\frac{0.3}{\left(\frac{xt}{c}\right)^2}\right) + \left(\frac{5a_0}{4(xt/c)^{3/2}}\right) + \left(\frac{1}{5p}\right) \tag{9}$$

$$a_3 = \left(\frac{0.1}{\left(\frac{xt}{c}\right)^3}\right) - \left(\frac{0.375a_0}{\left(\frac{xt}{c}\right)^{5/2}}\right) + \left(\frac{1}{10p\left(\frac{xt}{c}\right)}\right) \tag{10}$$

Having the t/c and I, r_{LE} can be calculated using Eq. (11). An index of 6 will result in the original NACA airfoil shape series and the index is recommended not to exceed 8 [75]. Further details on the modification of the shape of the NACA 4-digit airfoil series is described in Refs. [75–78].

$$r_{LE} = 0.5[0.296904((t/c)/0.2)(I/6)]^2 = 0.5[((t/c)/0.2)a_0]^2 \tag{11}$$

3.3. Naming scheme

In this work, which is focused on symmetric airfoils with zero camber, the following scheme is used to name the airfoils: "*NACA00t/c − I/xt/c*", where the symbols in the order of appearance are:

- t/c is the airfoil relative maximum thickness as percent of the chord
- I is the leading-edge radius index (with one decimal precision)
- xt/c is the chordwise position of the airfoil maximum thickness in tenths of the chord (with two decimal precision)

As an example, the NACA0018–4.5/2.75 airfoil has $t/c = 18\%c$, $I = 4.5$, and $xt/c = 27.5\%$.

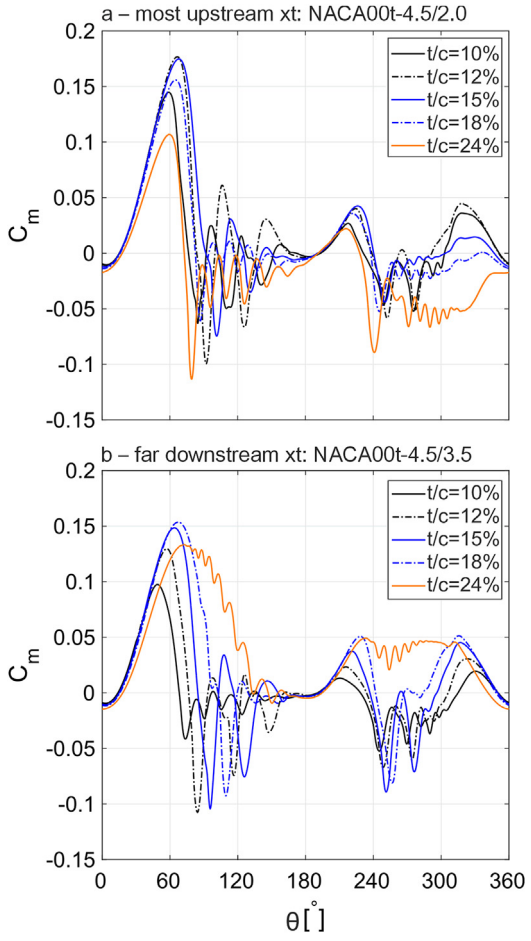

Fig. 8. Turbine instantaneous moment coefficient during the last revolution for selected airfoils ($\lambda = 2.5$).

4. Results

The results are classified in three sub-sections, i.e. Sec. 4.1–4.3, where the impact of the three parameters (*t/c, xt/c and I*), are separately discussed. In Sec. 4.4, the overall combined impact of the airfoil shape parameters on the turbine power performance is presented. The analysis is performed at two different λ of 2.5 and 3.0, where at both λ the variations of α exceeds the static stall angle for all the studied airfoils and the blade experiences deep dynamic stall. Fig. 6 shows the variations of α during the turbine last revolution at $\lambda = 2.5$ and 3.0, where the variations of α are more limited for $\lambda = 3.0$. Please note that the values of the angle of attack are directly calculated from the CFD results, applying the method completely described in Ref. [69].

4.1. Impact of maximum thickness (t/c)

Fig. 7 shows the turbine C_P versus t/c for different values of xt/c. The plots correspond to three different values of $I = 4.5$, 6.0 and 7.5 (low, moderate and high values), at $\lambda = 2.5$ and 3.0. Fig. 8 shows the turbine instantaneous moment coefficient (C_m) during the last revolution for selected airfoils. It can be seen that:

When the turbine is operating at $\lambda = 2.5$:

Regarding the airfoils with I = 4.5 (see Fig. 7a): For the airfoils with $xt/c = 20\%$–30%, a polynomial trend is observed for C_P versus t/c. When t/c increases from 10% to 24%, an initial growth in C_P values is observed. Following that, an optimal t/c (t_{opt}/c) exists within the studied range at which the C_P reaches its maximum value ($C_{P,max}$). The t_{opt}/c is found to gradually increase when xt/c shifts downstream towards the trailing edge up to 30%. Higher values of t_{opt}/c for the airfoils with larger xt/c implies that the further downstream the xt/c is, the thicker the optimal airfoil shape is. For $xt/c = 20\%$, 22.5%, 25%, 27.5% and 30%, t_{opt}/c is 12%, 15%, 18%, 18% and 21%, respectively. Note that increasing t/c also means increasing the pressure gradient along the airfoil, therefore, to optimally introduce higher favorable pressure gradient along the airfoil a longer chordwise extent is shown to be needed. By increasing t/c, the absolute difference between $C_{P,max}$ and the corresponding C_P value for the thinnest airfoil ($t/c = 10\%$) increases. Such a value for the airfoils with $xt/c = 20\%$, 22.5%, 25%, 27.5%, and 30% is 0.0254, 0.0426, 0.0585, 0.0672 and 0.0751, respectively. The higher $C_{P,max}$ values for the thicker blades at their corresponding optimal xt/c (xt_{opt}/c) is due to the higher level of pressure gradient. This is in good agreement with the results of the earlier studies which concluded that thicker blades show a better performance than thinner airfoils [47]. The observed polynomial trend for C_P versus t/c can be explained as follows. For a fixed xt/c within the discussed range, when t/c increases to the optimal value, at which $C_{P,max}$ occurs, the stall on the blade is postponed. This can be seen, for example, in Fig. 8a where the sudden drop in C_m occurs at comparatively higher azimuthal angles when t/c increases from 10% to 12%. Note that within the range at which $t/c \leq t_{opt}/c$, the slope of the $C_l - \alpha$ curve remains almost invariant to t/c. On the contrary, when $t/c > t_{opt}/c$, the stall on the blade is promoted, the slope of the $C_l - \alpha$ curve and the $C_{l,max}$ value drop and the chordwise extent of the trailing-edge separation substantially grows due to the higher adverse pressure gradient for $X > xt/c$. The comparatively earlier stall can be recognized from the C_m plots shown in Fig. 8a, where the t/c increases from 12% to 24%.

In contrast to the observed trend for $xt/c \leq 30\%$, for the higher values of $xt/c = 35\%$ and 40%, the C_P monotonically grows yielding the $C_{P,max}$ at the highest thickness of $t/c = 24\%$. The absolute difference between the $C_{P,max}$ and the corresponding C_P value for the thinnest airfoil ($t/c = 10\%$) for the airfoils with $xt/c = 35\%$ and 40% is 0.0657 and 0.083, respectively. The monotonic increase in C_P with t/c is because for the xt/c positions of 35% and 40%, by increasing t/c the stall on the blade is found to be delayed and the dynamic stall and the consequent loads fluctuations are alleviated for thicker airfoils. This can be seen, for example, in Fig. 8b, where increasing t/c from 10% to 18% results in substantial delay in the sudden drop in C_m and an increase in the curve peak. By further increase of the t/c to 24% the C_m drop is altered to a more gradual reduction with more limited fluctuations due to the diminished dynamic stall. For the thicker airfoils, e.g. $t/c = 24\%$, (although the slope of the $C_l - \alpha$ curve, the peak in C_m plot and the $C_{l,max}$ values are lower) the more gradual trailing-edge stall results in significantly lower C_d values, which eventually is reflected as higher turbine C_P. Note that due to the large amount of presented results, the C_l and C_d plots are not shown and only the turbine C_m plot is shown in Fig. 8.

Regarding the airfoils with I = 6.0 (see Fig. 7b): Similar trend to that of the smallest I of 4.5 is observed, except that the C_P shows a less sensitivity to t/c. The variations of the C_P when t/c changes is relatively less, compared to $I = 4.5$, especially for higher values of xt/c. Note that the t_{opt}/c for the airfoils with $xt/c = 20\%$ and 25% is 15%, which is a bit different than that of lower I. The impact of I on the observed reduction in $|\Delta C_P|$ is separately discussed in Sec. 4.3, thus not elaborated here.

Regarding the airfoils with I = 7.5 (see Fig. 7c): The overall trend for $C_P - t/c$ is similar to those of $I = 4.5$ and 6.0, although the corresponding $|\Delta C_P|$ shows noticeably less sensitivity to t/c. For the airfoils with $xt/c = 20\%$, 22.5%, 25%, 30%, 35% and 40%, the t_{opt}/c are 12%, 12%, 15%, 18%, 21% and 15%, respectively.

When the turbine is operating at $\lambda = 3.0$:

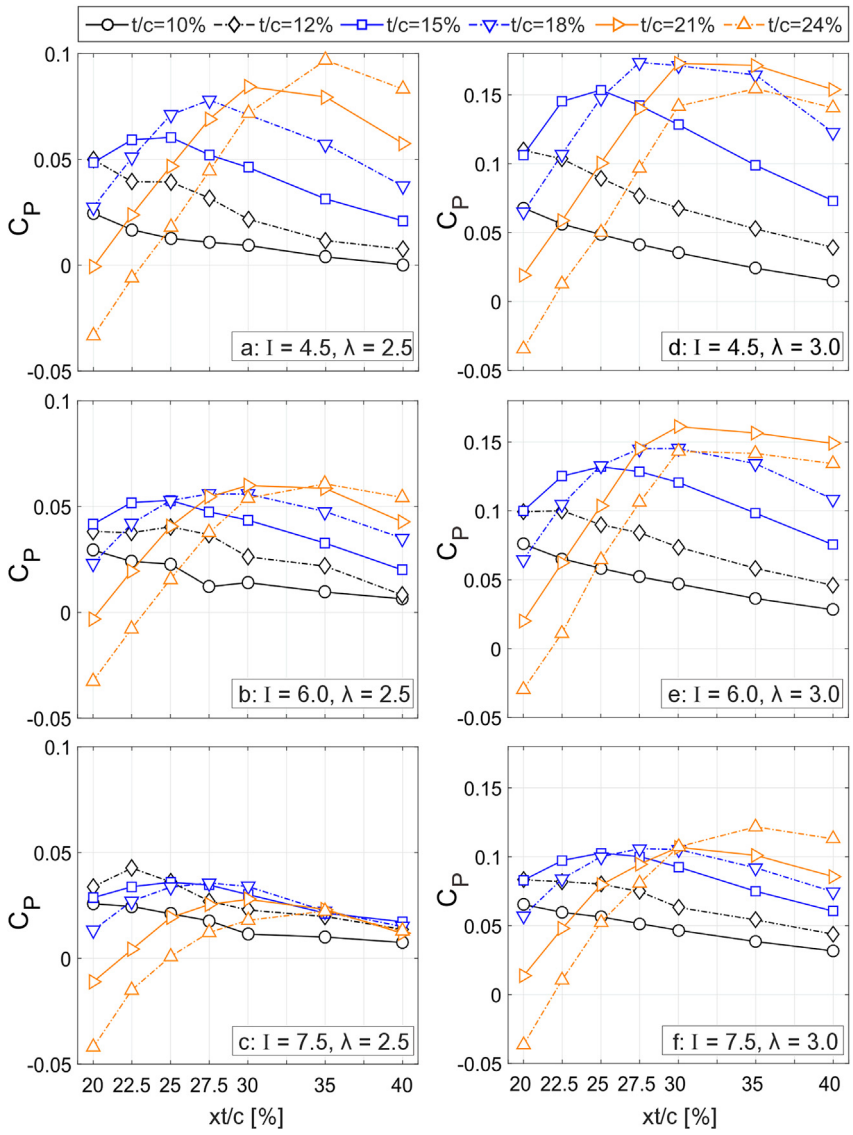

Fig. 9. Turbine power coefficient versus chordwise position of maximum thickness.

Regarding the airfoils with $I = 4.5$ (see Fig. 7d): The overall trend observed for $C_P - t/c$ is very similar to that of the lower λ of 2.5, except a noticeable difference that is the C_P is found to be significantly more sensitive to t/c, leading to comparatively higher values of $|\Delta C_P|$ at $\lambda = 3.0$. This can be explained as follows. Varying t/c modifies the pressure gradient distribution along the blade, which influences the laminar-to-turbulent transition onset and consequently the aerodynamic loads. In the post-stall regime, however, as the flow over the blade is fully separated, therefore, modification of t/c will have negligible effect. When λ increases from 2.5 to 3.0, the variation of α reduces, see Fig. 6, and the blade experiences the post-stall regime within a more limited azimuthal range. Because of that, the regime within which the t/c and the boundary layer events are influential expands and this is reflected as the observed higher sensitivity of the C_P to t/c at $\lambda = 3.0$. Apart from this, the trend for the $xt/c = 35\%$ and 40%, which is monotonic at $\lambda = 2.5$ within the studied range, now is changed to polynomial having an optimal t/c of 21%.

Regarding the airfoils with $I = 6.0$ (see Fig. 7e): The overall trend for $C_P - t/c$ is similar to both those of the same I at the lower λ of 2.5, and the smallest I of 4.5 at the same $\lambda = 3.0$. However, the C_P is comparatively less sensitive to t/c (lower values of $|\Delta C_P|$) compared to that of $I = 4.5$ at the same $\lambda = 3.0$ and is found to be noticeably more sensitive to t/c, compared to $I = 4.5$ at $\lambda = 2.5$.

Regarding the airfoils with $I = 7.5$ (see Fig. 7f): The C_P follows the same trend as those of the smallest and moderate I of 4.5 and 6.0 at the same $\lambda = 3.0$, but with comparatively less sensitivity to t/c. However, comparing to that of the same $I = 4.5$ at $\lambda = 2.5$, the $|\Delta C_P|$ is considerably more sensitive to t/c, especially for the airfoils with higher xt/c.

4.2. Impact of chordwise position of maximum thickness (xt/c)

Fig. 9 depicts the C_P versus the xt/c for different values of t/c. It can be seen that, when the turbine is operating at $\lambda = 2.5$:

Regarding the airfoils with $I = 4.5$ (see Fig. 9a): For the thinnest airfoils with $t/c = 10\%$ and 12%, the $C_{P,max}$ corresponds to the airfoil with t/c positioned at $xt/c = 20\%$. By increasing xt/c from 20% to 40%, the C_P value monotonically decreases. The absolute reduction in C_P when xt/c shifts downstream from 20% to 40% is 0.0243 and 0.0424 for $t/c = 10\%$ and 12%, respectively. The reduction in C_P by increasing xt/c occurs because the stall of the thinnest airfoils is originated

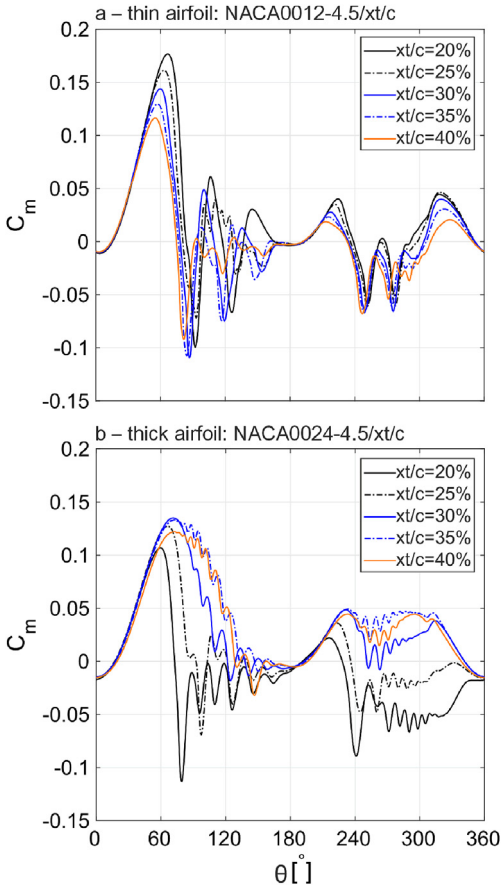

Fig. 10. Turbine C_m during the last revolution at $\lambda = 2.5$ for selected airfoils.

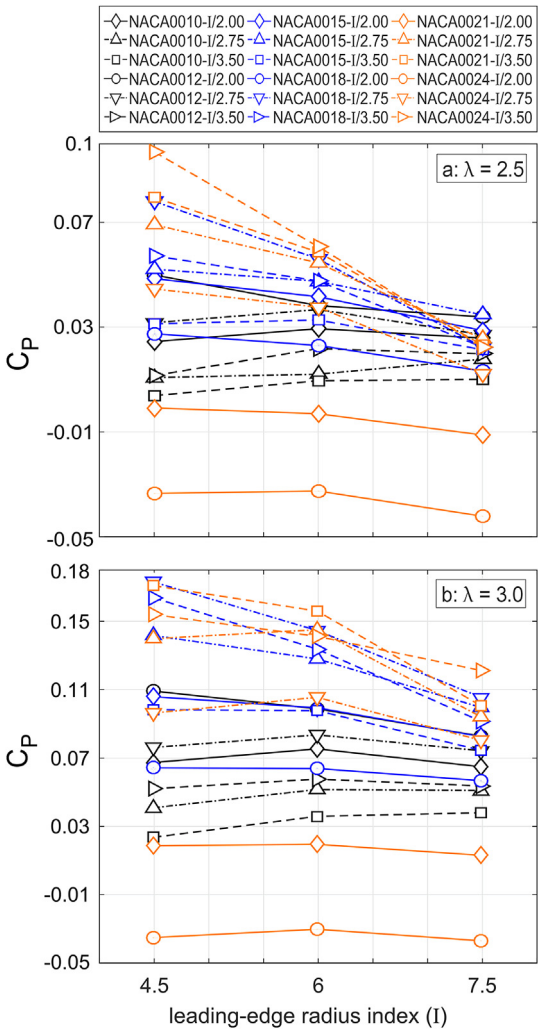

Fig. 11. Turbine power coefficient versus leading-edge radius index for selected airfoils.

from the leading edge and shifting xt/c towards trailing edge promotes the flow separation resulting in an earlier stall on the blade (earlier drop in C_l and jump in C_d). This can be observed from the C_m plots shown in Fig. 10a, where for the airfoil with $t/c = 12\%$, when xt/c increases from 20% to 40%, the sudden drop in C_m, which signals the occurrence of stall, happens at a comparatively earlier θ and also the peak value of C_m reduces.

Conversely for the thicker airfoils with $t/c \geq 15\%$, a polynomial trend is observed for $C_P - xt/c$. For these airfoils, when xt/c increases higher than 20%, an initial growth in C_P values is observed. Following that, an optimal xt/c (xt_{opt}/c) exists within the studied range corresponding to $C_{P,max}$. The xt_{opt}/c is found to increase when the airfoils become thicker meaning that, the optimal shape corresponds to positioning of the t/c at a further downstream xt/c. This was earlier discussed in Sec. 4.1. For $t/c = 15\%$, xt_{opt}/c is 25%. By further increasing of t/c to 18%, 21% and 24%, xt_{opt}/c shifts downstream to 27.5%, 30% and 35%. The absolute difference in $C_{P,max}$ (at xt_{opt}/c) with respect to the corresponding C_P value at $xt/c = 20\%$ for the airfoils with $t/c = 15\%$, 18%, 21% and 24% is 0.0119, 0.0505, 0.0852 and 0.1303, respectively. This polynomial trend can be explained as the stall of these thicker airfoils mainly originates from the trailing edge [79–82]. Therefore, shifting xt/c further downstream to xt_{opt}/c limits the chordwise extent of the adverse pressure gradient region along the airfoil, which eventually delays the stall and limits the trailing-edge separation, reduces the post-stall load fluctuations and the drag jump. For the thickest airfoils with $t/c \geq 21\%$, the stall type shifts to a softer one and the post-stall fluctuations are significantly alleviated for $xt/c \geq 35\%$. This can be seen from the C_m plots for the thickest airfoil with $t/c = 24\%$ (Fig. 10b), where for higher values of xt/c the turbine C_m improves, the sudden drop in C_m changes to a more gradual reduction and the subsequent C_m fluctuations (observed at θ values after the drop in C_m), get less pronounced. The peak in C_m also shifts from $\theta = 60°$ at $xt/c = 20\%$ to $\theta = 72°$ at $xt/c = 40\%$ (see Fig. 10b). Alleviation of the stall for the discussed airfoils also results in higher C_m values in the rotor aft half, $180° \leq \theta < 360°$. Further increase of $xt/c > xt_{opt}/c$, is found to promote the stall.

Regarding the airfoils with $I = 6.0$ (see Fig. 9b): The observed trend for $C_P - xt/c$ is very similar to that of $I = 4.5$ and the xt_{opt}/c for airfoils with different thickness remain the same. However, the sensitivity of the C_P to the xt/c is more limited as the magnitude of variations in C_P when xt/c changes is comparatively less, especially for the thicker airfoils. Detailed discussion on the impact of I on the observed reduction in $|\Delta C_P|$ is separately presented in Sec. 4.3, thus not elaborated here.

Regarding the airfoils with $I = 7.5$ (see Fig. 9c): The observed trend for the thinnest airfoils with $t/c = 10\%$ and for the thicker airfoils with $t/c > 12\%$, is similar to those of $I = 4.5$ and 6.0. For the airfoils with $t/c = 12\%$, xt_{opt}/c is slightly shifted, i.e. 22.5%. In addition, $|\Delta C_P|$ is found to be noticeably less when xt/c varies.

When the turbine is operating at $\lambda = 3.0$:

Regarding the airfoils with $I = 4.5$ (see Fig. 9d): The overall trend

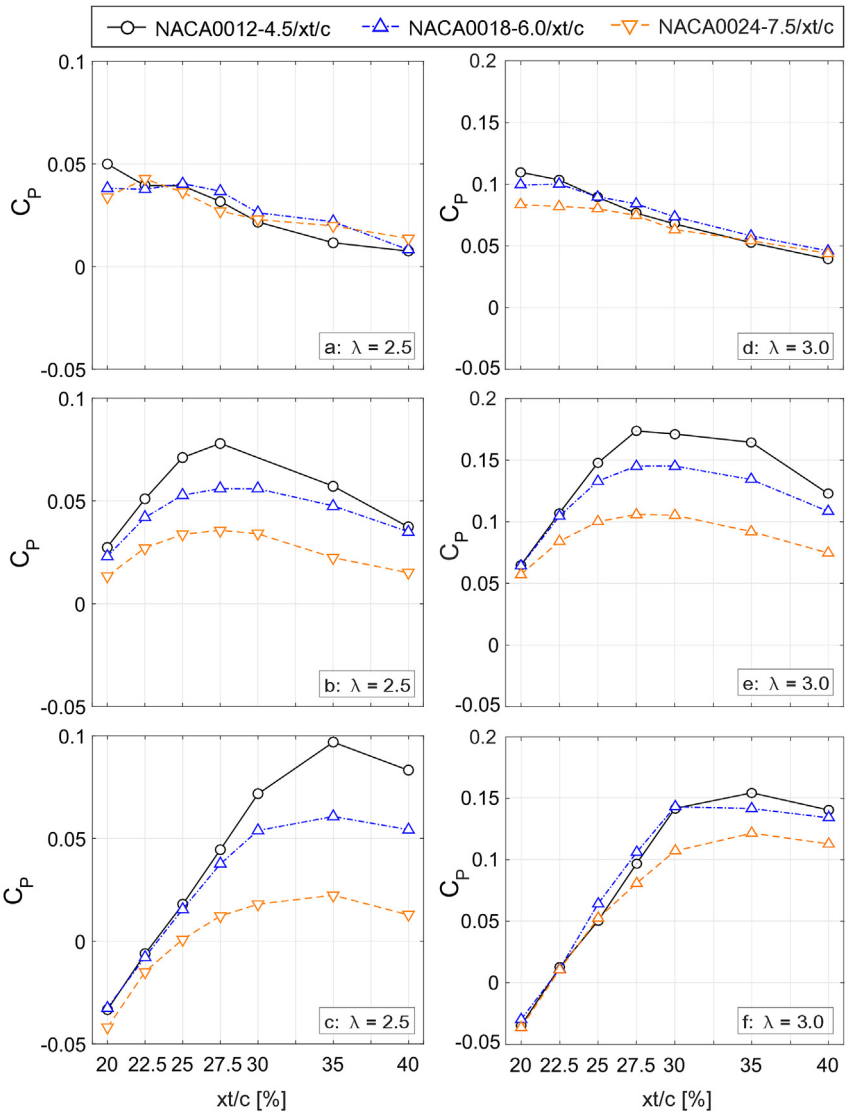

Fig. 12. Turbine power coefficient versus chordwise position of maximum thickness (xt/c) for selected airfoils with different leading-edge radius index (I).

for $C_P - xt/c$ is similar to that of the same I at the lower λ of 2.5, except the fact that the C_P is comparatively more sensitive to xt/c (higher values of $|\Delta C_P|$ are observed) at λ = 3.0, at which the variation of α is less than that of λ = 2.5 (see Fig. 6). This higher sensitivity can be explained with the same physical reasoning presented in Sec. 4.1 that is briefed as follows. Varying xt/c modifies the airfoil pressure gradient distribution, thus influencing the transition onset and aerodynamic loads. For λ = 3.0, the variation of α reduces (see Fig. 6) and the blade experiences the post-stall regime within a more limited azimuthal range, thus expanding the regime within which the variation of the xt/c is influential. This causes the comparatively higher sensitivity of the C_P to xt/c at λ = 3.0. Although the xt_{opt}/c for airfoils with different thickness remain the same, the $C_{P,max}$ value for the thickest airfoil with $t/c = 24\%$ no longer is higher than that of the airfoil with $t/c = 21\%$, in contrast to the trend observed at λ = 2.5. The fact that at higher λ, the comparatively thinner airfoil of $t/c = 21\%$ outperforms the thicker airfoil of $t/c = 24\%$ is because, in general, thicker airfoils have comparatively lower slope of the $C_l - \alpha$ curve but higher stall angle and softer stall. Therefore, if the variations of α reduces (higher λ), then what matters most is the superior performance at lower α and this is where the slope of the $C_l - \alpha$ curve matters more. This results in the superior performance of the thinner 21%c airfoil over the thicker 24%c airfoil.

Regarding the airfoils with $I = 6.0$ (see Fig. 9e): The results for C_P versus xt/c follow a trend similar to those of the same leading-edge radius at the lower λ of 2.5, and also the smallest I of 4.5 at the same λ. However, the C_P is noticeably more sensitive to xt/c (higher values of $|\Delta C_P|$) compared to that of the same leading-edge radius at λ = 2.5 and is found to be comparatively less sensitive to xt/c (lower values of $|\Delta C_P|$) compared to that of $I = 4.5$ at λ = 3.0.

Regarding the airfoils with $I = 7.5$ (see Fig. 9f): The same trend as those of $I = 4.5$ and 6.0, but with relatively less sensitivity to xt/c is observed. Nevertheless, comparing to that of the same leading-edge radius of $I = 4.5$ at lower λ of 2.5, $|\Delta C_P|$ when xt/c changes is considerably more, especially for the thicker airfoils.

4.3. Impact of leading-edge radius index (I)

Fig. 11 shows the C_P versus I for airfoils with different t/c and xt/c at λ = 2.5 and 3.0. Fig. 12 shows the C_P versus xt/c for a thin, a moderately-thick and a thick airfoil. Fig. 13 presents the C_m during

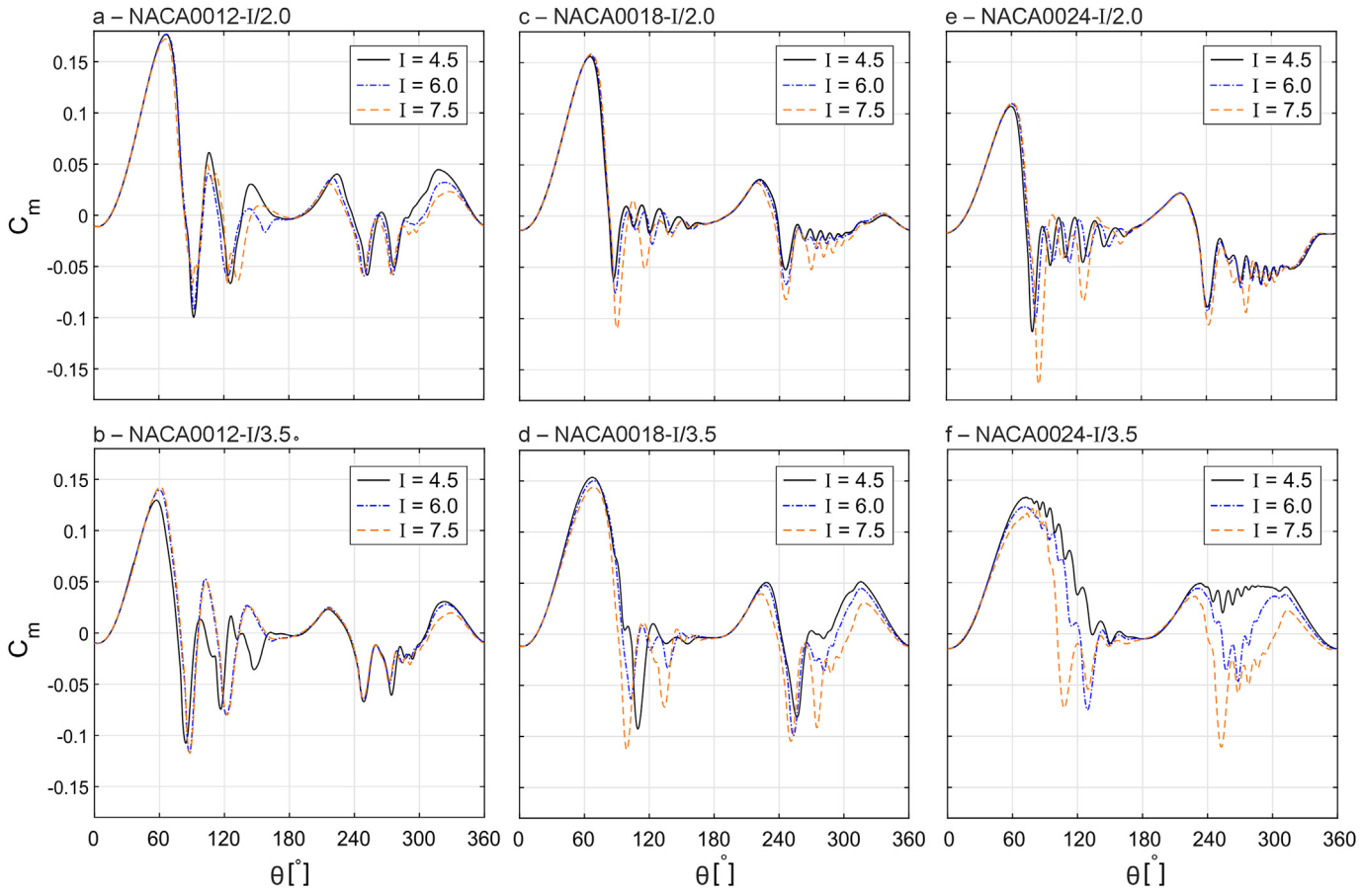

Fig. 13. Turbine C_m during the last revolution at $\lambda = 2.5$ for selected airfoils with different I.

Table 6
Impact of leading-edge radius index on C_P for NACA0021-I/3.0.

λ	2.5			3.0		
I	7.5	6.0	4.5	7.5	6.0	4.5
C_P	0.028	0.06	0.084	0.107	0.16	0.173
ΔC_P [%]	+114.7	+41		+50.7	+7.2	

the last turbine revolution for the selected airfoils at $\lambda = 2.5$. The observations for these figures are categorized based on *t/c* as follows.

Regarding the airfoils with t/c ≤ 12% (see Figs. 11 and 12a,d and 13a-b): In general, the C_P values of the thin airfoils are found to be weakly dependent on the leading-edge radius. This can be explained as changing *I* will minimally modify the airfoil shape for thin airfoils due to the geometrical constraints set by the maximum thickness, thus the aerodynamic loads are marginally influenced by *I*. For $xt/c = 20\%$, by increasing *I* from 4.5 to 7.5, the C_P value slightly decreases. The absolute difference in C_P for the airfoil with $I = 4.5$ with respect to the corresponding value at $I = 6.0$ and 7.5 is 0.012 and 0.016, respectively. This small reduction in C_P is also consistent with the observed trend for the C_m plots for the thin airfoils with different *I*, see Fig. 13a. The analysis shows that by increasing *I* for the thin airfoils, the $C_{d,max}$ slightly increases resulting in the observed marginal reduction in C_P. This is while the slope of the $C_l - \alpha$ curve and the α_{stall} remain almost unchanged and a light increase in $C_{l,max}$ for higher values of *I* is observed. The impact of *I* on the C_P remains marginal for the thinner airfoils with *xt/c* further downstream as well. Similar trend is observed at the higher λ of 3.0, where the C_P is weakly sensitive to *I*.

Regarding the airfoils with 15% ≤ t/c ≤ 18% (see Figs. 11 and 12b,e and 13c-d): The observed trend for $C_P - I$ is different from that of the thinner airfoils. Firstly, the C_P values are found to monotonically decrease by increasing *I*, regardless of the *t/c* and *xt/c*. This is thought to be due to the increase in the $C_{d,max}$ for higher values of *I*. Secondly, the C_P values are more significantly sensitive to *I*, compared to the thinner airfoils. This could be explained as the comparatively higher *t/c* of these airfoil imposes less geometrical constraints and changing the leading-edge radius can more noticeably influence the airfoil shape, compared to the thinner airfoils. The higher sensitivity of C_P to *I* is more prominent for moderate values of *xt/c*, $22.5\% \leq xt/c \leq 35\%$. This range approximately corresponds to the optimal C_P range for such airfoils and the highest sensitivity of C_P to *I* is observed at the $C_{P,max}$. The absolute differences between the $C_{P,max}$ values for NACA0018-*I*/2.75 when *I* increases from 4.5 to $I = 6.0$ and 7.5 are 0.022 and 0.0423. The C_P values are less dependent to *I* for the airfoils where $xt/c < 22.5\%$ or $>35\%$. This can also be seen in Fig. 13c where for the airfoils with $xt/c = 20\%$, the turbine C_m and the azimuthal angle corresponding to the sudden drop in C_m are almost invariant to *I*. Conversely, the peak in the C_m plots for airfoils with $xt/c = 35\%$, see Fig. 13d, decrease by increasing *I*, which is in line with the observed trend for C_P values. Similar trend, as explained for the $\lambda = 2.5$, is observed at the higher λ of 3.0, where the C_P is even more sensitive to *I*. The higher λ corresponds to the operational regime where the moderate-thickness airfoil perform better and have higher $C_{P,max}$. Thus, the impact of *I* is found to be the most significant in the C_P regime. This is interesting because as already discussed, the impact

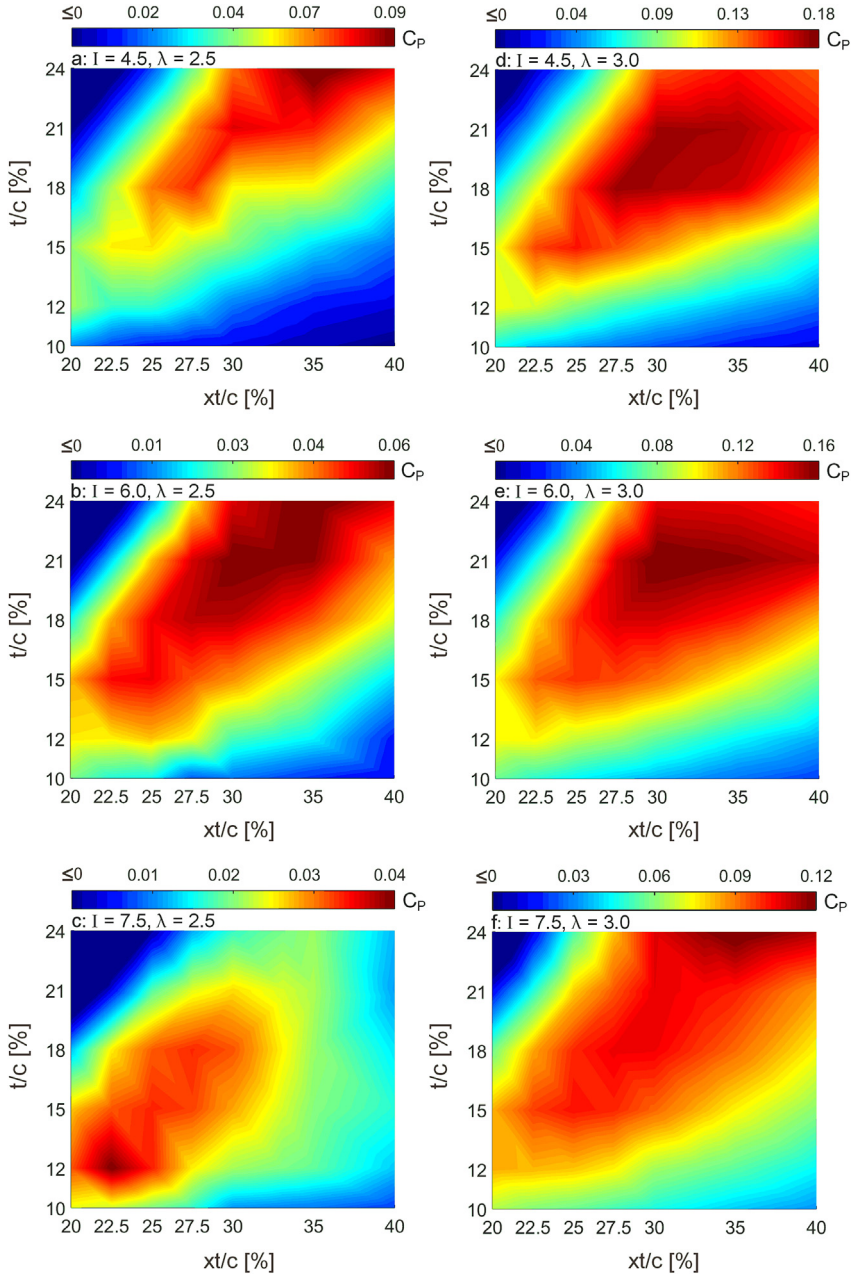

Fig. 14. Turbine C_P in t/c − xt/c space. Each contour plot is based on 42 simulations. Note the difference in range of colormaps.

Table 7
Optimal airfoil shapes for λ = 2.5 and 3.0.

λ	Name	*t/c* [%]	*xt/c* [%]	*I* [−]
2.5	NACA0024−4.5/3.5	24	35	4.5
3.0	NACA0018−4.5/2.75	18	27.5	4.5

of the *I* is also more significant at moderate values of *xt/c*, corresponding to the optimal values. Below it is shown that for the thicker airfoils where the optimal regime is slightly shifted, the range of most prominent influence of *I* is similarly shifted.

Regarding the airfoils with t/c > 18% (see Figs. 11 and 12c,f and 13e-f): The observations for the thicker airfoils are quite similar to those of the moderate-thickness airfoils. The C_P is found to monotonically decrease by increasing *I*. Table 6 gives an example for the airfoil NACA0021-*I*/3.0, where the increase in C_P by reduction in *I* is quantified. In addition, the highest sensitivity of C_P to *I* is found to occur at the optimal range of *xt/c*, which for thick airfoils correspond to larger values of *xt/c*, and at the lower λ of 2.5, which also corresponds to the operational regime where the thick airfoils have their best performance. The absolute differences between the $C_{P,max}$ values at λ = 2.5 for NACA0024-*I*/3.5 when *I* increases from 4.5 to *I* = 6.0 and 7.5 are 0.0362 and 0.0745. The C_m plots for NACA0024-*I*/3.5 shown in Fig. 13f also imply the reduction in the C_m values, the promotion in the occurrence of stall, the more significant post-stall load fluctuations and the dramatic reduction in the C_m value in the turbine downwind quartile for higher values of *I*. In addition, Increasing *I* is found to reduce the slope of the $C_l - \alpha$ curve and the drag jump due to stall (due to a more subtle stall). For small values of *xt/c* the airfoil shape and thus the aerodynamic loads are

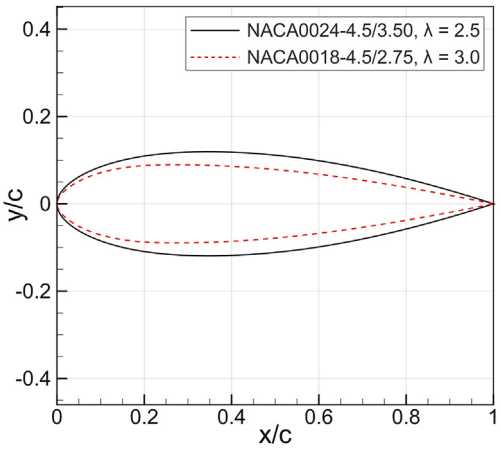

Fig. 15. Optimal airfoil shapes for λ = 2.5 and 3.0.

insignificantly sensitive to *I*. As can be seen, for example, in Fig. 13e, the turbine C_m and the instant of the stall occurrence are almost invariant to *I*.

4.4. Overall impact of airfoil shape

This section gives an overall view of the combined impact of the airfoil shape on the turbine C_P and C_T at the λ of 2.5 and 3.0 in deep dynamic stall.

Fig. 14 illustrates the C_P values in $t/c - xt/c$ space for different *I* and λ. At both λ, the global optimum corresponds to the smallest *I* of 4.5. At the lower λ of 2.5, where the variations of α are higher, the global optimum occurs at higher *t/c* and *xt/c*, compared to the λ of 3.0. Increasing λ, results in reduction in the range of variations of α, which influences the global optimum, by decreasing the optimal values of *t/c* and *xt/c*. Table 7 lists the characteristics of the optimal airfoils at both λ and the optimal airfoils are illustrated in Fig. 15. The dependency of the global optimal airfoil characteristics shows the significance of the fact that the airfoil design needs to be with careful considerations regarding the target operational conditions of the turbine.

At $\lambda = 2.5$, for the smallest leading-edge radius, $I = 4.5$, the optimal combination of *t/c* and *xt/c* correspond to the top right corner of the contour plot, i.e. high thickness with *xt/c* far from leading edge. Increasing *I* is found to shift the local optimum diagonally to the bottom left corner of the contour plot. For $I = 4.5$, the local optimum corresponds to a thick airfoil, $t/c = 24\%$, with $xt/c = 35\%$. For $I = 6.0$, the local optimum corresponds to relatively thick airfoils with *xt/c* relatively far from the leading edge, where both optimal values of *t/c* and *xt/c* are comparatively less than that of the $I = 4.5$. For $I = 7.5$, the optimal shape corresponds to a thin airfoil with *xt/c* close to the leading edge. The dependency of the local optimum on all the 3 shape defining parameters is an important finding as it reveals their combined influence and confirms the initial hypothesis that an airfoil shape study of one of the parameters while keeping the rest fixed could be misleading by not presenting the overall picture.

At $\lambda = 3.0$, the local optimum at different leading-edge radius is less significantly shifted, which implies that where the variations of α are more limited, the optimal shape could be less sensitive to the *I*. Overall, the local optimum at different values of *I* correspond to moderate to high values of *t/c* and *xt/c*.

The contour plots help to identify the region in which optimal airfoil characteristics lie, while also revealing the regions of the poor turbine C_P, which need to be avoided. Such plots may aid as a conceptual reference for VAWT designers and manufacturers to make the right decisions in the initial design stages, so that they can achieve the desired goals.

Fig. 16 illustrates the turbine C_T values in $t/c - xt/c$ space for different *I* at λ = 2.5 and 3.0. An important observation is that the regions of highest C_T are not coinciding with the local optimums in C_P plots. The $C_{T,max}$ regions are, consistently for all values of *I* and λ, corresponding to the bottom left corner of the plots, i.e. thin airfoils with *t/c* positioned near the leading edge. This inconsistency in the regions of the optimal C_P and the $C_{T,max}$ is of significant importance and is contrary to the typical observations for the HAWTs. Typically for HAWTs, where the turbine exerts higher thrust loads on the flow, it can also extract more energy, therefore, the optimal points for C_P and C_T are correlated, within a range. However, the underlying physics of VAWTs is different, and a direct correlation between the C_P and C_T values are not present. Therefore, the C_T values are of less importance when analyzing the turbine power performance and could be more relevant to the structural analysis of the turbine and tower. Nevertheless, increasing *I* is found to increase the extent of the region of high C_T values. In addition, the turbine experiences higher C_T values at higher λ of 3.0.

4.5. Aerodynamic analysis of optimal airfoils

Fig. 17 shows the aerodynamic load coefficients, namely lift and drag coefficients C_l and C_d, versus θ and angle of attack α during the turbine last half-revolution for the optimal airfoil shapes at λ = 2.5 and 3.0, which are NACA0024−4.5/3.5 and NACA0018−4.5/2.75, respectively. For both cases, the occurrence of dynamic stall is apparent with post-stall load fluctuations, load hysteresis, the lift drops and the drag jump. The optimal airfoils have a $C_{l,max}$ of nearly 1.5. The drag jump is less substantial at the higher λ of 3.0, where the range of variation of α is more limited and the airfoil experiences comparatively lighter dynamic stall.

Fig. 18 illustrates contour plots of the dimensionless instantaneous tangential velocity ($V_{tan,n}$) with superimposed streamlines at selected azimuthal positions for the optimal airfoils. On top of the figure the coordinate system and the presented azimuthal positions are schematically shown. The figure is presented to highlight the reverse flow regions along the optimal airfoil shapes. For both optimal airfoils, the airfoil experiences a trailing-edge type of stall, i.e. the stall is originated from a trailing-edge separation (TES) which gradually grows towards the leading-edge and eventually covers the whole suction side. For the NACA0024−4.5/3.5 at λ = 2.5, the TES is formed at θ = 65°. By further increase of θ to 75°, a counter-rotating trailing-edge roll-up vortex (TEV) is forming which grows larger at θ = 85° and is shed. This initiates the load fluctuations observed in C_l and C_d plots. By shedding the TEV, at θ = 95°, again only the TES is observed. At higher θ, again, the TEV can be seen, which signals the repeated formation and shedding of the TEV and the consequent load fluctuations in Fig. 17. At the same time, the TES is growing and covers the whole blade at θ = 125°, where the highest drag is also experienced. The process of stall for NACA0018−4.5/2.75 at λ = 3.0 is quite similar but the presence of TEVs is less pronounced, which explains the milder load fluctuations.

5. Discussion

The presented results in Sec. 4 correspond to two different tip

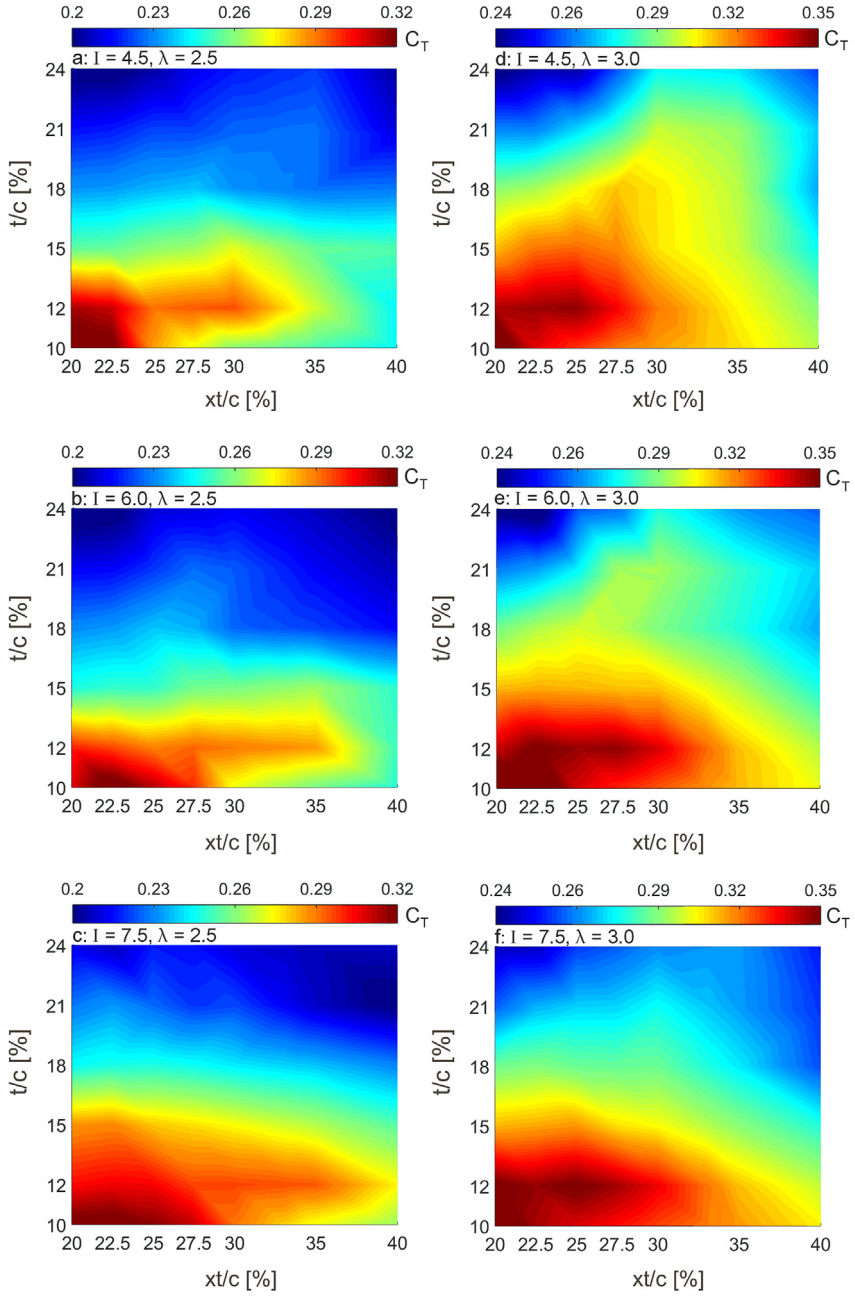

Fig. 16. Turbine C_T in t/c − xt/c space. Each contour plot is based on 42 simulations. Note the difference in range of colormaps.

speed ratios of 2.5 and 3, where the turbine blade experiences deep dynamic stall, with different range of variations of the angle of attack. The analysis highlights the dependency of the optimal airfoil shape to the turbine tip speed ratio, i.e. the range of variation of α. This dependency suggests the importance of continuation of this work for other tip speed ratios, where a light dynamic stall would occur, or dynamic stall is avoided. In addition, the study is performed at a fixed Reynolds number, turbulence intensity and reduced frequency, where the variance of the optimal airfoil characteristics to these operational parameters is also of interest for future studies.

Airfoil asymmetry, which is described by airfoil maximum camber and its chordwise position, is another important geometrical characteristic impacting the power performance of VAWTs, which is yet to be comprehensively investigated in future studies towards designing optimal airfoil shapes for VAWTs.

In addition, the airfoil shape modification is based on the NACA 4-digit airfoil series, which are the most popular choices for VAWTs. This choice allowed us to change several geometrical parameters, namely maximum thickness (t/c), chordwise-position of maximum thickness (xt/c) and the leading-edge radius index (I), simultaneously.

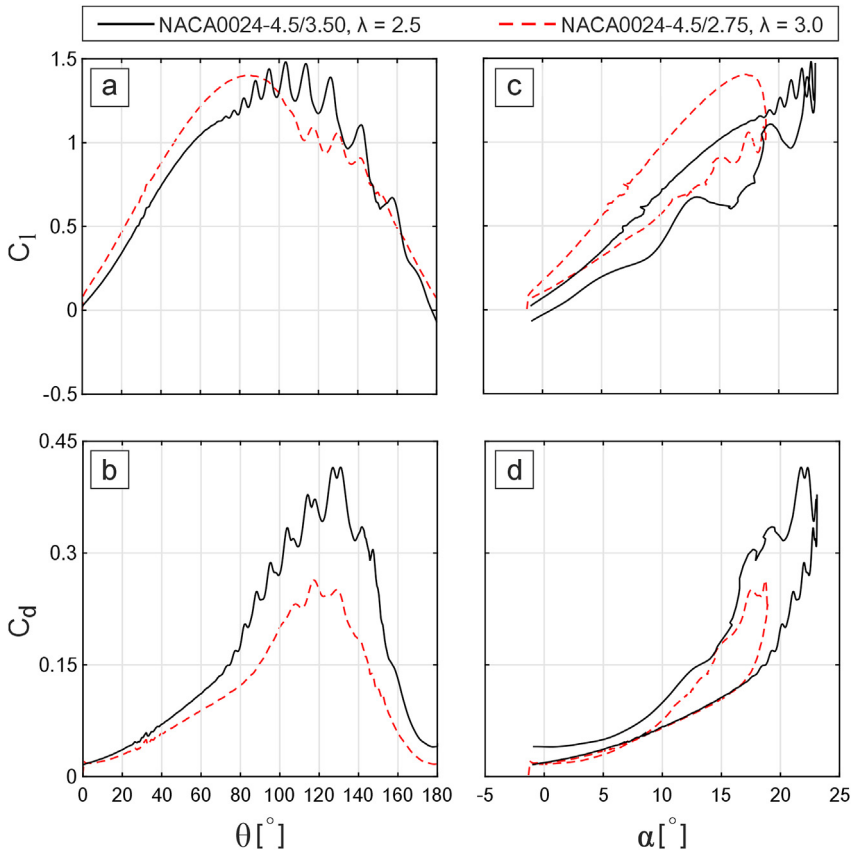

Fig. 17. Variations of lift and drag coefficients versus azimuth and angle of attack during the last turbine half-revolution for the optimal airfoil shapes, i.e. NACA0024−4.5/3.50 and NACA0018−4.5/2.75 at λ = 2.5 and 3.0.

The focus of the analysis in the present study is on the analysis of the turbine power performance under the influence of the aforementioned airfoil shape defining parameters. However, other parameters, such as the blade surface roughness, turbine solidity and the number of blades (esp. for high solidity turbines) could also influence the airfoil aerodynamic loads and thus could impact the choice of the optimal airfoil shape. Therefore, the sensitivity of the identified optimal regions for the airfoil characteristics to these parameters could be interesting to be investigated.

Furthermore, while designing a turbine, aerodynamic performance is one of the objectives, and the blade structural performance and the turbine noise generation could be other important factors one should consider. A design challenge is to compromise all considering the dictated design constraints. Therefore, the choice of the airfoil shape also needs to consider other factors such as the blade structural strength and stiffness, which are of importance to withstand the high aerodynamic loads and to limit the resultant deflections, and the blade aeroacoustic noise.

6. Conclusions

Incompressible URANS simulations, extensively validated with experiments, are employed to characterize the impact of parameters defining the shape of the symmetric airfoils, namely *t/c*, *xt*/c and *I*, on the power performance of VAWTs in dynamic stall regime, at λ = 2.5 and 3.0.

Within the studied ranges, the main conclusions are as follows:

- Depending on the airfoil leading-edge radius, an optimal combination of *t/c* and *xt/c* exists, corresponding to $C_{P,max}$. Increasing *t/c*, shifts the optimal *xt/c* towards the trailing edge. In addition, by increasing *t/c* (i.e. thicker airfoils), the C_P becomes more significantly sensitive to *xt/c*.
- At λ = 2.5, increasing *I* from 4.5 to 7.5 shifts the optimal combination of *t/c* and *xt/c* from high values, i.e. thick airfoils with *xt/c* far from the leading edge, to low values, i.e. thin airfoils with *xt/c* near the leading edge. At the higher λ of 3.0, the optimal combination of *t/c* and *xt/c* is less dependent on the leading-edge radius.
- Decreasing *I* from the default value for NACA 4-digit airfoil series, *I* = 6.0, to 4.5 monotonically increases the turbine C_P, regardless of the *t/c* and *xt/c*. The increment becomes more pronounced near the optimal value of *xt/c* for the respective airfoil and in general where C_P is highest. The improvement in the C_P is mainly due to the reduction in drag jump associated with stall.
- The optimal airfoil characteristics is dependent on the turbine λ, i.e. the range of variations of α. At the lower λ of 2.5, the optimal airfoil is a thick airfoil, *t/c* = 24%, with *xt/c* far from the leading edge at 35%, and the airfoil has a comparatively small leading-edge radius with *I* = 4.5 (NACA0024−4.5/3.5). The optimal shape changes to NACA0018−4.5/2.75 for the higher λ of 3.0.

The findings of the present study are of high significance as they highlight the coupled influence of the three symmetric airfoil shape-defining parameters on the turbine power performance. This means that, investigating one parameter, while keeping the rest fixed, could be misleading and will not provide the overall picture failing to identify the global optimum. In addition, the identified optimal airfoil shapes at dynamic stall can be a starting point for

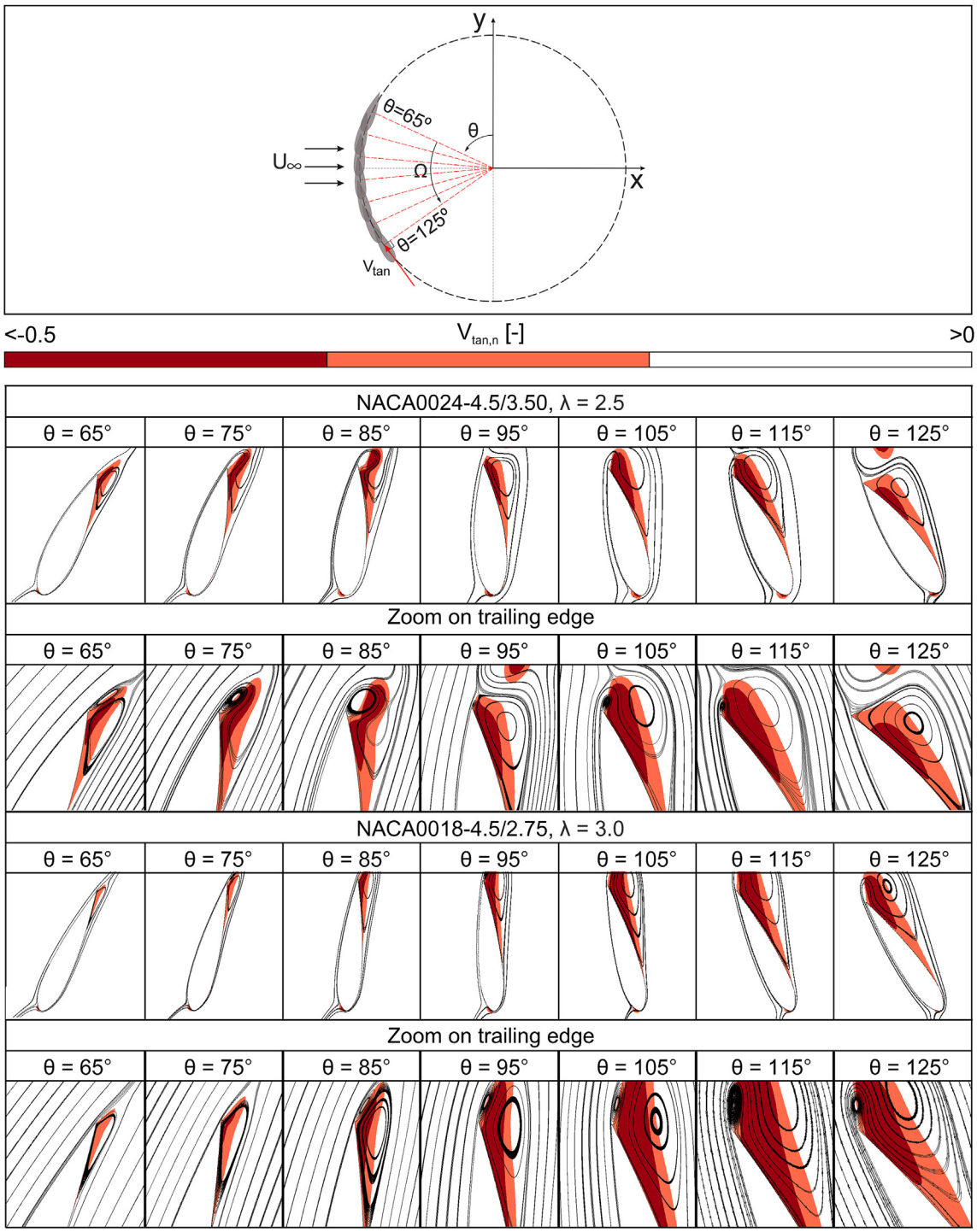

Fig. 18. Contour plots of the dimensionless instantaneous tangential velocity with superimposed streamlines. The coordinate system and the presented azimuthal positions are schematically shown on top.

defining a set of shapes for designing morphing airfoils for VAWTs.

CRediT authorship contribution statement

M. Rasoul Tirandaz: Conceptualization, Methodology, Software, Validation, Formal analysis, Investigation, Resources, Data curation, Writing – original draft, Visualization, Funding acquisition. **Abdolrahim Rezaeiha:** Conceptualization, Methodology, Validation, Writing – review & editing, Visualization, Supervision, Project administration.

Declaration of competing interest

The authors declare that they have no known competing financial interests or personal relationships that could have appeared to influence the work reported in this paper.

Acknowledgement

The first author acknowledges the support from his home university for the use of supercomputing facilities. The second author is currently a postdoctoral fellow of the Research Foundation – Flanders (FWO) and is grateful for the financial support (project FWO 12ZP520N).

References

[1] M. Aoki, H. Nishimura, E. Yamakawa, Effect of Airfoil on rotational noise of helicopter rotor, in: Aircraft Symposium vol. 33, Hiroshima, Japan, 1995.
[2] M.A. McVeigh, F.J. McHugh, Influence of tip shape, chord, blade number, and airfoil on advanced rotor performance, J. Am. Helicopter Soc. 29 (4) (1984) 55–62.
[3] J.J. Thibert, J. Pouradier, Design and test of an helicopter rotor blade with evolutive profile, in: 12 Th Congress of the International Council of the Aeronautical Sciences ICAS, 1980 (Munich, Germany).
[4] A. Gopalarathnam, C. McAvoy, Effect of airfoil aharacteristics and trim considerations on aircraft performance, in: 19th AIAA Applied Aerodynamics Conference, 2001 (Anaheim, CA, U.S.A).
[5] A. Gopalarathnam, C.W. McAvoy, Effect of airfoil characteristics on aircraft performance, J. Aircraft 39 (3) (2002) 427–433.
[6] W. Letko, J.D. Brewer, Effect of Airfoil Profile of Symmetrical Sections on the Low-Speed Rolling Derivatives of 45 Degree Sweptback-Wing Models of Aspect Ratio 2.61, National Advisory Committee for Aeronautics, Washington, D.C, 1949.
[7] R.M. Wood, D.S. Miller, Impact of airfoil profile on the supersonic aerodynamics of delta wings, J. Aircraft 23 (9) (1986) 695–702.
[8] N. Teja, et al., Optimization of micro air vehicle airfoil, IJRET 5 (3) (2016) 217–219.
[9] L. Zhao, S. Yang, Influence of thickness variation on the flapping performance of symmetric NACA airfoils in plunging motion, Math. Probl Eng. 2010 (2010) 19.
[10] K.A. Ismail, C.V. Rosolen, Effects of the airfoil section, the chord and pitch distributions on the aerodynamic performance of the propeller, J. Braz. Soc. Mech. Sci. Eng. 41 (3) (2019) 1–19.
[11] E.N. Jacobs, Characteristics of Propeller Sections Tested in the Variable Density Wind Tunnel, NACA-TR-259, National Advisory Committee for Aeronautics, U.S.A., 1928, pp. 125–140.
[12] H. Zhang, Y. Hu, G. Wang, The effect of aerofoil camber on cycloidal propellers, AEAT 90 (8) (2018) 1156–1167.
[13] S. Abraham, et al., Effect of airfoil shape and turning angle on turbine airfoil aerodynamic performance at transoniccConditions, in: ASME 2011 International Mechanical Engineering Congress and Exposition, 2011. Denver, Colorado, USA.
[14] T.C. Nash, Gas Turbine Engine Turbine Blade Airfoil Profile, Raytheon Technologies Corp: U.S.A, 2015.
[15] S. Abbasi, A. Joodaki, Effect of blade profile on the performance characteristics of axial compressor in design condition, JCARME 9 (2) (2020) 287–296.
[16] A.M. Group, A. Carter, Blade profiles for axial-flow fans, pumps, compressors, etc, Proc. Inst. Mech. Eng. 175 (1) (1961) 775–806.
[17] M. Schnoes, E. Nicke, A database of optimal airfoils for axial compressor throughflow design, J. Turbomach. 139 (5) (2017), 051008.
[18] A. Shrum, C. LaMaster, Airfoil Shape for a Compressor, General Electric Co: U.S.A, 2009.
[19] I. Akmandor, K. Ekici, Airfoil analysis for horizontal axis wind turbines, in: ASME Wind Energy Symposium. 1998, AIAA, Reno, NV, U.S.A., 1998, p. 20.
[20] F. Bertagnolio, et al., Wind Turbine Airfoil Catalogue, Risoe-R-1280(EN): Risø National Laboratory, Denmark, 2001.
[21] Dahl, K.S. and P. Fuglsang, *Design of the Wind Turbine Airfoil Family RISØ-A-XX*. 1998: Risoe-R-1024(EN), Risø National Laboratory, Denmark.
[22] P. Fuglsang, C. Bak, Development of the Risø wind turbine airfoils, Wind Energy 7 (2) (2004) 145–162.
[23] P. Giguere, M.S. Selig, New airfoils for small horizontal axis wind turbines, J. Sol. Energy Eng. 120 (2) (1998) 108–114.
[24] B. Kanya, K. Visser, The impact of airfoil selection on the design of small horizontal axis wind turbines, in: 48th AIAA Aerospace Sciences Meeting Including the New Horizons Forum and Aerospace Exposition, 2010. Orlando, Florida, U.S.A.
[25] Tangler, J.L. and D.M. Somers, *NREL Airfoil Families for HAWTs*. 1995, TP-442-7109, National Renewable Energy Lab.: Golden, CO, U.S.A.
[26] W. Timmer, R. Van Rooij, Summary of the Delft University wind turbine dedicated airfoils, J. Sol. Energy Eng. 125 (4) (2003) 488–496.
[27] R. van Rooij, N. Timmer, Design of Airfoils for Wind Turbine Blades, TU Delft, Faculty CiTG, The Netherlands, 2004.
[28] A. Bjorck, Coordinates and Calculations for the FFA-Wl-Xxx, FFA-W2-Xxx, FFA-W2-Xxx and FFA-W3-Xxx Series of Airfoils for Horizontal axis Wind Turbines, Technical Report FFA Tn., Stockholm, 1990.
[29] S. Sahebzadeh, A. Rezaeiha, H. Montazeri, Towards optimal layout design of vertical-axis wind-turbine farms: double rotor arrangements, Energy Convers. Manag. 226 (C) (2020) 113527.
[30] A. Rezaeiha, H. Montazeri, B. Blocken, A framework for preliminary large-scale urban wind energy potential assessment: roof-mounted wind turbines, Energy Convers. Manag. 214 (C) (2020) 112770.
[31] Y. Kato, K. Seki, Y. Shimizu, Vertical axis wind turbine designed aerodynamically at Tokai University, Period. Polytech. - Mech. Eng. 25 (1) (1981) 47–56.
[32] P.C. Klimas, Tailored Airfoils for Vertical axis Wind Turbines, Sandia National Laboratories, Albuquerque, NM, USA, 1984. Technical Report SAND84-1062.
[33] R. Galbraith, F. Coton, D. Jiang, Aerodynamic Design of Vertical axis Wind Turbines, GU Aero Report 9246. Department of Aerospace Engineering, University of Glasgow, Scotland, 1992.
[34] M. Claessens, The design and testing of airfoils for application in small vertical axis wind turbines, in: Faculty of Aerospace Engineering, Delft University of Technology, 2006.
[35] C.S. Ferreira, B. Geurts, Aerofoil optimization for vertical-axis wind turbines, Wind Energy 18 (8) (2015) 1371–1385.
[36] B. Hand, G. Kelly, A. Cashman, Aerodynamic design and performance parameters of a lift-type vertical axis wind turbine: a comprehensive review, Renew. Sustain. Energy Rev. 139 (2021), 110699.
[37] S. Zanforlin, Advantages of vertical axis tidal turbines set in close proximity: a comparative CFD investigation in the English channel, Ocean. Eng. 156 (2018) 358–372.
[38] M. Abkar, Theoretical modeling of vertical-axis wind turbine wakes, Energies 12 (1) (2018) 10.
[39] M. Elkhoury, et al., Wind tunnel experiments and delayed detached eddy simulation of a three-bladed micro vertical axis wind turbine, Renew. Energy 129 (2018) 63–74.
[40] A. Sagharichi, M. Zamani, A. Ghasemi, Effect of solidity on the performance of variable-pitch vertical axis wind turbine, Energy 161 (2018) 753–775.
[41] A. Ebrahimi, M. Movahhedi, Power improvement of NREL 5-MW wind turbine using multi-DBD plasma actuators, Energy Convers. Manag. 146 (2017) 96–106.
[42] C.S. Ferreira, et al., Visualization by PIV of dynamic stall on a vertical axis wind turbine, Exp. Fluid 46 (1) (2009) 97–108.
[43] B. Hand, G. Kelly, A. Cashman, Numerical simulation of a vertical axis wind turbine airfoil experiencing dynamic stall at high Reynolds numbers, Comput. Fluids 149 (2017) 12–30.
[44] K. Mulleners, M. Raffel, The onset of dynamic stall revisited, Exp. Fluid 52 (3) (2012) 779–793.
[45] A. Rezaeiha, H. Montazeri, B. Blocken, CFD analysis of dynamic stall on vertical axis wind turbines using Scale-Adaptive simulation (SAS): comparison against URANS and hybrid RANS/LES, Energy Convers. Manag. 196 (2019) 1282–1298.
[46] A. Rezaeiha, H. Montazeri, B. Blocken, CFD investigation of separation control on a vertical axis wind turbine: steady and unsteady suction, J. Phys. Conf. 1618 (2020), 052019.
[47] J. Healy, The influence of blade thickness on the output of vertical axis wind turbines, Wind Eng. 2 (1) (1978) 1–9.
[48] P. Migliore, Comparison of NACA 6-series and 4-digit airfoils for Darrieus wind turbines, J. Energy 7 (4) (1983) 291–292.
[49] B. Kirke, L. Lazauskas, Enhancing the performance of vertical axis wind turbine using a simple variable pitch system, J. Wind Eng. (1991) 187–195.
[50] G. Bedon, et al., Computational assessment of the DeepWind aerodynamic performance with different blade and airfoil configurations, Appl. Energy 185 (2) (2017) 1100–1108.
[51] M. Jafari, A. Razavi, M. Mirhosseini, Effect of airfoil profile on aerodynamic performance and economic assessment of H-rotor vertical axis wind turbines, Energy 165 (2018) 792–810.
[52] A. Meana-Fernández, et al., Parametrical evaluation of the aerodynamic performance of vertical axis wind turbines for the proposal of optimized designs, Energy 147 (2018) 504–517.
[53] C. Ferreira, et al., Comparison of aerodynamic models for vertical axis wind turbines, J. Phys. Conf. 524 (2014), 012125.
[54] M. Mohamed, Performance investigation of H-rotor Darrieus turbine with new airfoil shapes, J. Energy 47 (1) (2012) 522–530.
[55] C.-C. Nguyen, P.-T. Tran, A numerical study of thickness effect of the symmetric NACA 4-digit airfoils on self starting capability of a 1kW H-type vertical axis wind turbine, IJMEA 3 (3) (2015) 7–16.
[56] A. Subramanian, et al., Effect of airfoil and solidity on performance of small scale vertical axis wind turbine using three dimensional CFD model, Energy 133 (2017) 179–190.
[57] C. Song, et al., Study on aerodynamic characteristics of Darrieus vertical axis wind turbines with different airfoil maximum thicknesses through computational fluid dynamics, Arabian J. Sci. Eng. 45 (2) (2020) 689–698.
[58] H.M.S.M. Mazarbhuiya, A. Biswas, K.K. Sharma, Blade thickness effect on the aerodynamic performance of an asymmetric NACA six series blade vertical axis wind turbine in low wind speed, Int. J. Green Energy 17 (2) (2020) 171–179.
[59] S. Jain, U.K. Saha, On the influence of blade thickness-to-chord ratio on dynamic stall phenomenon in H-type Darrieus wind rotors, Energy Convers. Manag. 218 (2020) 113024.
[60] J. Chen, et al., Performance improvement of a vertical axis wind turbine by comprehensive assessment of an airfoil family, Energy 114 (2016) 318–331.
[61] Y. Wang, et al., Investigation on aerodynamic performance of vertical axis wind turbine with different series airfoil shapes, Renew. Energy 126 (2018) 801–818.

[62] D. Ragni, C.S. Ferreira, G. Correale, Experimental investigation of an optimized airfoil for vertical-axis wind turbines, J. Wind Energy 18 (9) (2015) 1629–1643.
[63] M.T. Asr, et al., Study on start-up characteristics of H-Darrieus vertical axis wind turbines comprising NACA 4-digit series blade airfoils, Energy 112 (2016) 528–537.
[64] C. Song, et al., Numerical investigation on the effects of airfoil leading edge radius on the aerodynamic performance of H-Rotor Darrieus vertical axis wind turbine, Energies 12 (19) (2019) 3794.
[65] G. Tescione, et al., Near wake flow analysis of a vertical axis wind turbine by stereoscopic particle image velocimetry, Renew. Energy 70 (2014) 47–61.
[66] A. Rezaeiha, H. Montazeri, B. Blocken, On the accuracy of turbulence models for CFD simulations of vertical axis wind turbines, Energy 180 (2019) 838–857.
[67] A. Rezaeiha, et al., Effect of the shaft on the aerodynamic performance of urban vertical axis wind turbines, Energy Convers. Manag. 149 (2017) 616–630.
[68] A. Rezaeiha, H. Montazeri, B. Blocken, Towards optimal aerodynamic design of vertical axis wind turbines: impact of solidity and number of blades, Energy 165 (2018) 1129–1148.
[69] A. Rezaeiha, H. Montazeri, B. Blocken, Characterization of aerodynamic performance of vertical axis wind turbines: impact of operational parameters, Energy Convers. Manag. 169 (2018) 45–77.
[70] A. Rezaeiha, H. Montazeri, B. Blocken, Scale-adaptive simulation (SAS) of dynamic stall on a wind turbine, in: Progress in Hybrid RANS-LES Modelling, Springer, 2020, pp. 323–333.
[71] A. Rezaeiha, H. Montazeri, B. Blocken, Towards accurate CFD simulations of vertical axis wind turbines at different tip speed ratios and solidities: guidelines for azimuthal increment, domain size and convergence, Energy Convers. Manag. 156 (2018) 301–316.
[72] P.J. Roache, Quantification of uncertainty in computational fluid dynamics, Annu. Rev. Fluid Mech. 29 (1997) 123–160.
[73] A. Rezaeiha, H. Montazeri, B. Blocken, Active flow control for power enhancement of vertical axis wind turbines: leading-edge slot suction, Energy 189 (2019) 116131.
[74] M.R. Castelli, A. Englaro, E. Benini, The Darrieus wind turbine: proposal for a new performance prediction model based on CFD, Energy 36 (8) (2011) 4919–4934.
[75] I.H. Abbott, A.E. Von Doenhoff, Theory of Wing Sections: Including a Summary of Airfoil Data, McGraw-Hill, New York, 1949.
[76] Pickering, K.A., Recovered Equations and Ordinates of the Göttingen 765 Airfoil.
[77] P.A. Henne, Applied Computational Aerodynamics. Progress in Astronautics and Aeronautics, vol. 125, American Institute of Aeronautics and Astronautics (AIAA), Washington, D.C., 1990.
[78] E.N. Jacobs, K.E. Ward, R.M. Pinkerton, The Characteristics of 78 Related Airfoil Sections from Tests in the Variable-Density Wind Tunnel, NACA Report 460, US Government Printing Office, 1933.
[79] W.J. McCroskey, The Phenomenon of Dynamic Stall, NASA TM 81264, NASA, Moffett Field CA. ARC, 1981.
[80] A. Sharma, M. Visbal, Numerical investigation of the effect of airfoil thickness on onset of dynamic stall, J. Fluid Mech. 870 (2019) 870–900.
[81] V.A. Frolov, Laminar separation point of flow on surface of symmetrical airfoil, in: Perm, Russia AIP Conference Proceedings., AIP Publishing LLC, 2016.
[82] J. Meseguer, et al., On the circulation and the position of the forward stagnation point on airfoils, Int. J. Mech. Eng. Educ. 35 (1) (2007) 65–75.